Rock Mechanics and Rock Engineering (2023) 56:2607–2631
https://doi.org/10.1007/s00603-022-03203-0

ORIGINAL PAPER

Experimental Study on Rockburst and Spalling Failure in Circular Openings for Deep Underground Engineering

Kai Ling[1,2] · Yang Wang[3,4,5] · Dongqiao Liu[1] · Yunpeng Guo[1,2] · Zheng Zhou[1,2] · Lulu Zhang[1,2] · Manchao He[1]

Received: 31 May 2022 / Accepted: 15 December 2022 / Published online: 31 December 2022

Abstract

This study aims to simulate the process of rockburst and spalling failure of roadway surrounding rock under three-dimensional stress in deep rock engineering. Utilizing an independently developed true triaxial rockburst experimental setup, the failure process of a circular tunnel under initial in-situ stress at a depth of 500 m was investigated using red sandstone with prefabricated holes. A miniature camera device and acoustic emission (AE) monitoring system were used to monitor and record the experimental process in real time. Using the collected data, the process of rockburst and spalling failure of the circular tunnel was reproduced. Finally, the difference between rockburst and spalling failure was analyzed and compared based on four aspects of stress characteristics, acoustic emission characteristics, fragment characteristics, and *V*-shaped notch morphology characteristics. The experimental results show that the failure of surrounding rock was more likely to occur under dynamic disturbance load, resulting in particle ejection. The spalling failure was found to be a slow and gradual static failure process. The mechanism of rockburst was more complex involving tension-shear coupling failure, whereas, the mechanism of spalling failure was simple involving a tensile failure. Compared with spalling failure, rockburst was more intense, producing more debris, and the *V*-shaped notch was narrow and deep.

Highlights

- Failure process of rockburst and spalling is reproduced in a laboratory.
- The stress characteristics of rockburst and spalling failure are calculated based on elastic theory.
- Frequency-amplitude characteristics and crack types based on acoustic emission are analyzed.
- The failure intensity of rockburst and spalling is investigated based on the rock fragments and morphology of *V*-shaped notch.
- The failure process of rockburst and spalling is discussed along with strain energy.

✉ Yang Wang
wy_successful@163.com

✉ Dongqiao Liu
liudongqiao@yeah.net

1 State Key Laboratory for GeoMechanics and Deep Underground Engineering, China University of Mining and Technology, Beijing 100083, China

2 School of Mechanics and Civil Engineering, China University of Mining and Technology, Beijing 100083, China

3 Institute of Geomechanics, Chinese Academy of Geological Sciences, Beijing 100081, China

4 Key Laboratory of Active Tectonics and Geological Safety, Ministry of Natural Resources, Beijing 100081, China

5 Research Center of Neotectonism and Crustal Stability, China Geological Survey, Beijing 100083, China

Keywords True triaxial test · Rockburst · Spalling failure · Acoustic emission · *V*-shaped notch

List of symbols

σ_H, σ_h, and σ_v	Two horizontal and a vertical in-situ stresses
γ	Bulk density
H	Burial depth
p and q	Vertical and average horizontal stresses
$\sigma_{\theta max}$	Maximum tangential stress
σ_{zi}	Initial sidewall failure stress
AF	Average frequency
RA	The ratio of rise time to amplitude
k	Slope of a boundary line
L_{eq}	Equivalent side length
L_{eqmax}	Maximum equivalent side length
N	The number of fragments whose equivalent side length is greater than L_{eq}
N_0	The number of fragments whose equivalent side length is L_{eqmax}
D	Fractal dimension
w and l	Width and length of fragments
d	The depth of *V*-shaped notch
β	The angle of *V*-shaped notch
$\sigma_{\theta 1}$, $\sigma_{\theta 2}$, and $\sigma_{\theta 3}$	Tangential stresses at different stages
$\Delta 1$ and $\Delta 2$	Increments of tangential stress
W	Strain energy
F_X, F_Y, and F_Z	Forces in the direction of X, Y, and Z
L_X, L_Y, and L_Z	Displacements in the direction of X, Y, and Z
V	Rock specimen volume
V_ε	Strain energy density
ΔE	Excess energy
E_0	Required energy for rock failure under the uniaxial compression test
E_1' and E_2'	Stored strain energy during the quiet period of rockburst and spalling failure
E_1'' and E_2''	Stored strain energy of rockburst and spalling failure when the initial failure occurred
E_1 and E_2	Stored strain energy when the rockburst or spalling failure occurs
ΔE_1 and ΔE_2	Excess energy of spalling failure and rockburst

1 Introduction

A large number of deep underground rock engineering projects such as mining, traffic tunnels, and diversion tunnels, have been started to fulfill the ever-growing needs of national economic construction and development. Due to the influence of a complex geological environment, engineering excavation disturbance, and other factors, rock masses in deep underground constructions showcase unconventional failure behavior, which is rarely seen in a shallow rock mass (Martin 1997). Depending on the physical properties of the rock mass as well as the loading conditions, failure can occur violently or gradually. Violent failure can be characterized as a brittle failure (i.e. a sudden loss of strength following little or no plastic deformation post-failure) or a rockburst when coupled with a rapid ejection. A gradual or non-violent failure can be characterized by spalling failure (i.e. non-violent brittle failure) (Keneti and Sainsbury 2018). Rockburst, a dynamic instability phenomenon, is characterized by fragments ejecting violently away from the surrounding rock and energy releasing abruptly (He et al. 2018), as shown in Fig. 1a. Spalling failure is characterized by thin plate-shaped rocks spalling from the surrounding rocks at low velocity, belonging to the static instability phenomenon (Hoek and Martin 2014), as shown in Fig. 1b. These incidents cause casualties and economic losses and pose threat to the deep rock engineering construction.

Researchers across the world have conducted several laboratory simulation studies to investigate the mechanism of spalling failure and rockburst in deep rock masses under extreme stresses. Lee and Haimson (1993) conducted true triaxial compression experiments on granite rock samples with prefabricated circular holes and found that cracks were densely distributed on both sidewalls and parallel to the sidewall, suggesting that spalling failure was mainly caused by tensile cracks. Qiu et al. (2014) studied the mechanism and evolution process of spalling failure using true triaxial loading and unloading experiments and discussed the severity of spalling failure based on the principle of energy balance. Hu et al. (2021) stated that spalling and buckling were two important stages of rock failure, and studied the influence of materials with different tensile strengths on the severity of the spalling failure. Su et al. (2020) studied the acoustic emission (AE) precursor characteristics of instability failure of coarse-grained granite under static or dynamic conditions. Ma and Liu (2022) analyzed the mechanism of slab collapse and the complex movement process of slab collapse by using the discontinuous deformation analysis (DDA) method. Li et al. (2017, 2018a, b) performed true triaxial unloading compression experiments to study the effects of different aspect ratios of a specimen and intermediate principal stresses on rock failure characteristics and found that unloading under true triaxial conditions would lead to spalling failure. Hidalgo and Nordlund (2012) compared laboratory test results with numerical simulation results to analyze the spalling failure process in hard rock. They further demonstrated that the crack initiation strain calculated in the laboratory test was related to the in-situ crack initiation strain.

In terms of the rockburst experiment, Liu et al. (2020) studied the temporal and spatial evolution characteristics of AE and thermal radiation characteristics of granite samples with a prefabricated circular hole under different confining pressures. He et al. (2012, 2015) carried out a true triaxial compression experiment by using cubic red sandstone with a hole in the middle and successfully simulated the rockburst phenomenon. Based on the observations, they concluded that the rockburst process occurred in three stages, i.e., vertical spalling, vertical slab buckling deformation, and rockburst damage. Gong et al. (2017, 2018, 2020; Gong and Si 2021) and Si et al. (2018, 2021) carried out a series of three-dimensional true triaxial compression experiments on red sandstone, marble, granite, and other rock samples with circular, rectangular, and *D*-shaped holes, and found that the laboratory test results were very similar to the in-situ rockburst characteristics. Zhao et al. (2020) performed triaxial compression experiments on sandstone specimens with a trapezoidal opening to study the influence of different lateral stresses on the rockburst process and failure characteristics. Zhang et al. (2019) used cubic granite with a circular hole to conduct a biaxial compression experiment to simulate the rockburst phenomenon, and studied the spectral characteristics and clustering characteristics of AE signals. Su et al. (2017a, b, 2018, 2019) used true triaxial test equipment to study the influence of loading rate, axial stress, radial stress, temperature, dynamic load frequency, and other factors on rockburst. Si et al. (2022a, b) investigated the rockburst process and characteristics of layered rock and sandstone under different stress states. Li et al. (2021) studied the mechanisms of structural-slip rockburst based on sound waves, acoustic emissions, and failure characteristics of the structural planes. He et al. (2021a, b, c) independently developed a novel high-pressure servo true triaxial rockburst equipment capable of multi-face unloading and conducted a double-faces unloading rockburst experiment on red sandstone to investigate the ejection velocity of rock fragments. Liu et al. (2021) carried out a double-face unloading rockburst experiment on bedding red sandstone and studied the anisotropic evolution process during rockburst.

The preceding studies have substantially advanced our understanding of spalling failure and rockburst in deep underground engineering, revealing the mechanism involved in spalling failure and rockburst. However, existing studies focus solely on either the spalling failure or the rockburst. According to Martin et al. (1999) and Du et al. (2016), there is a strong correlation between spalling failure and rockburst in surrounding rock, wherein, spalling failure is closely related to the triggering of rockburst. Diederichs (2007) stated that spalling failure of surrounding rock can occur before the rockburst, leading to unstable deformation of the approximately parallel rock slabs produced by the spalling, which creates conditions for the energy sudden release of rockburst. At present, very limited works concerning the relation between spalling failure and rockburst have been conducted. Thereby, this study presents two types of rock failure experiments using red sandstone with a prefabricated circular hole to investigate the commonalities and differences between spalling failure and rockburst. In addition, miniature cameras and AE monitoring systems were equipped to monitor and record the process of spalling failure and rockburst. The results are analyzed in detail with a focus on exploring the commonalities and differences between spalling failure and rockburst.

2 Experimental Design

2.1 Rock Specimen

The specimens were selected from red sandstone with good integrity and texture. The specimens were processed into cubic blocks of size $110 \times 110 \times 50$ mm^3 with circular holes (Φ50 mm), as shown in Fig. 2. The uniaxial compressive

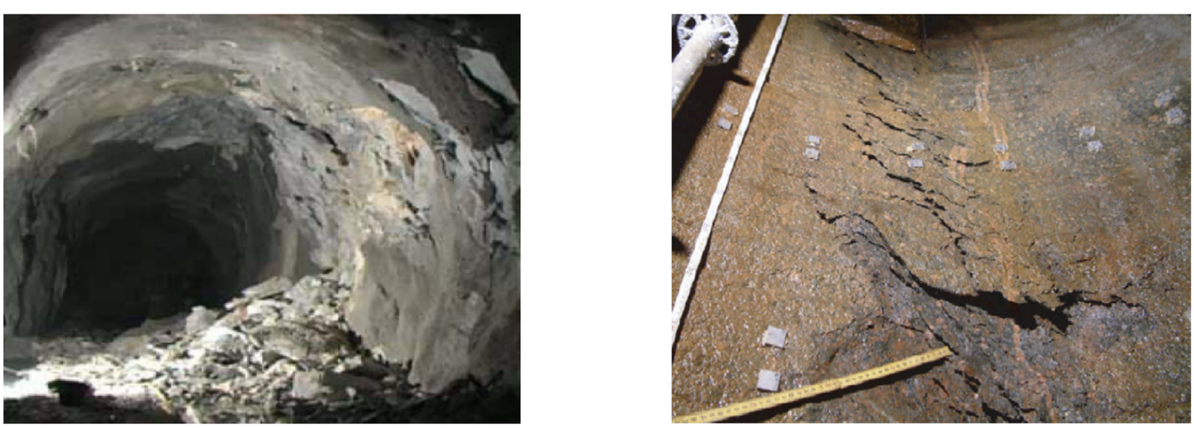

(a) Rockburst (He et al. 2012)   (b) Spalling failure (Martin and Christiansson, 2009)

Fig. 1 Two typical failure modes of the surrounding rock

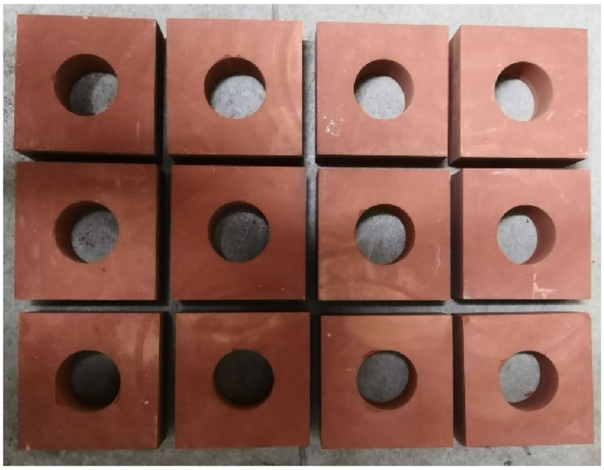

(a) Photograph of red sandstone

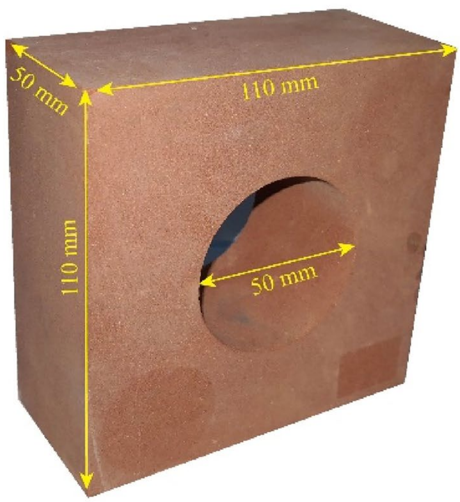

(b) Schematic illustration of sample size

Fig. 2 Experimental sample

strength, elastic modulus, and Poisson's ratio of red sandstone were 87.07 MPa, 17.38 GPa, and 0.21, respectively. To reduce the experimental error, the surface flatness of the specimens was controlled at ± 0.05 mm, and the deviation of the verticality between adjacent surfaces was ± 0.25°. X-ray diffraction results show that the main mineral composition of sandstone was quartz (63.7%), calcite (13.1%), plagioclase (7.0%), potash feldspar (2.6%), hematite (1.9%), and clay minerals (11.7%).

2.2 Test Equipment

The experiment was carried out using an independently developed true triaxial rockburst test system, which mainly included a servo controller, main engine, specimen box, and hydraulic power source. The equipment can simulate rockburst caused by dynamic disturbance load. The maximum load capacity of the equipment was 500 kN, the loading accuracy of force was 0.5 kN/s, and the loading accuracy of displacement was 0.004 mm/s. During the loading process, the force and displacement were dynamically recorded in real time. Micro-II AE monitoring system which is developed by PAC Company was used in the experiment to simultaneously monitor AE signals in the rockburst and spalling failure. The sampling frequency and sampling length were 2 Msps and 4 k, respectively, i.e., 2 M data points were collected every second and 4096 data points were registered for every AE elastic wave. Both preamplifier parameters and acquisition threshold was set as 40 dB to eliminate the electrical, instrumental, and environmental noises. Two wideband sensors with a resonant frequency of 0–1 MHz were used in the experiment and glued to the rigid plate. The experimental equipment is shown in Fig. 3.

The sample was in a true triaxial state throughout the experiment. To observe the failure process in the circular hole, a special rigid plate was designed to record real-time visual data. The special rigid plate contains a circular hole of the same size as the sample. A miniature camera device was installed inside the rigid plate, and the shooting direction was aligned with the axis of the hole. Since the sample was in a closed environment during the testing, a light source was added to illuminate the inside of the circular hole to facilitate the observation of experimental phenomena. Figures 4 and 5 show the real-time video acquisition and schematic diagram of the miniature camera device installation.

2.3 Experimental Scheme

In the present study, the initial ground stress was calculated using the empirical formula developed by Huang et al. (2013) to predict ground stress in North China. The relation between in-situ stress and depth is as follows:

$$\begin{cases} \sigma_H = 0.0233H + 4.6 \\ \sigma_h = 0.0162H + 2.1 \\ \sigma_v = \gamma H \end{cases} \tag{1}$$

where σ_H is the maximum horizontal principal stress (MPa), σ_h is the minimum horizontal principal stress (MPa), σ_v is the vertical stress (MPa), γ is the bulk density ($\gamma = 27$ kN/m^3) and H is the depth of the tunnel. The three-dimensional stress at 500 m was calculated as $\sigma_H = 16.3$ MPa, $\sigma_v = 13.6$ MPa, and $\sigma_h = 10.2$ MPa.

The maximum horizontal stress in practical tunnel design is generally parallel to the tunnel's axial direction, thus σ_H is set parallel to the axial direction of the circular hole. Two loading schemes were designed in this study

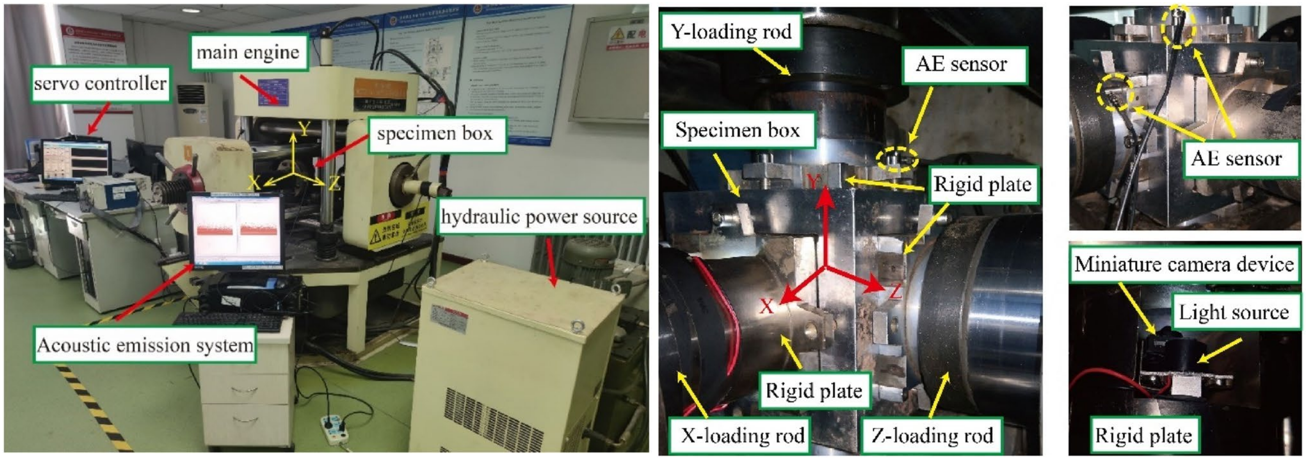

Fig. 3 True triaxial rockburst test system

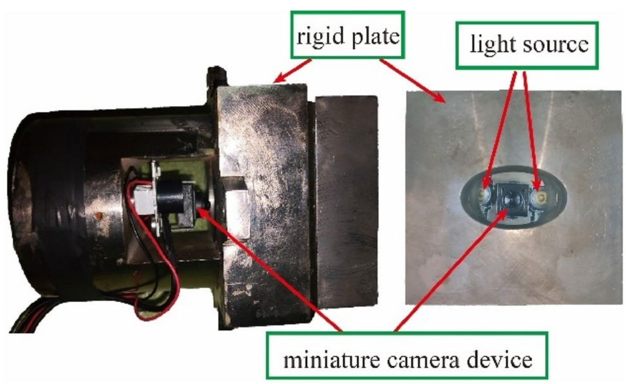

Fig. 4 Real-time video acquisition device

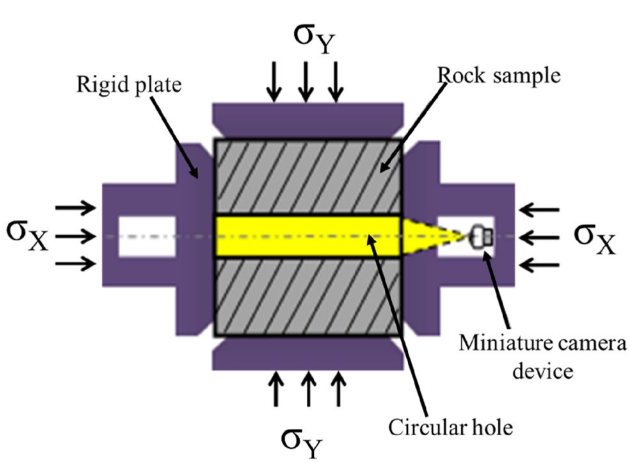

Fig. 5 Schematic diagram of miniature camera device installation

to analyze the rockburst induced by dynamic disturbance load and spalling failure caused by the static load. Firstly, the initial stress level was synchronously loaded at 0.5 kN/s in the *X*, *Y*, and *Z* directions. Once the initial stress level was attained, the load was maintained constant for 60 s. Static load or dynamic disturbance load was then continuously applied in the *Y* direction using displacement control to simulate spalling failure or rockburst, respectively. The triaxial stresses, σ_H, σ_v, and σ_h, of the rock sample, correspond to the *X*, *Y*, and *Z* directions of the true triaxial rockburst test system, respectively.

Dynamic and static experiments were classified according to the strain rate of the load applied. The distinction between quasi-dynamic experiments and the static experiment was approximately marked at 5×10^{-4} s^{-1} (Cai et al. 2007a). In this experiment, ramp disturbance was selected as the dynamic disturbance load. Considering the loading capacity of the equipment, the dynamic disturbance rate was set as 0.5 mm/s (i.e., the strain rate was 4.5×10^{-3} s^{-1}), which falls in the range of the dynamic loading. The static loading rate was set as 0.004 mm/s (i.e., the strain rate was 3.6×10^{-5} s^{-1}). Based on the above description, the schematic diagram of the loading path is shown in Fig. 6. The same experiment was repeated thrice to reduce random error and representative samples were selected for analysis and description.

3 Experimental Results

3.1 Test Curves

Figure 7 shows the actual loading stress path curves of rockburst and spalling failure. During the test, the contact area of the rigid plate with the specimen in the *X* direction was larger than that in the *Y* and *Z* directions (the contact area in the *X* direction was about 1.01×10^{-2} m^2, and in the *Y*, and *Z* directions was 5.5×10^{-3} m^2). However, since the loading

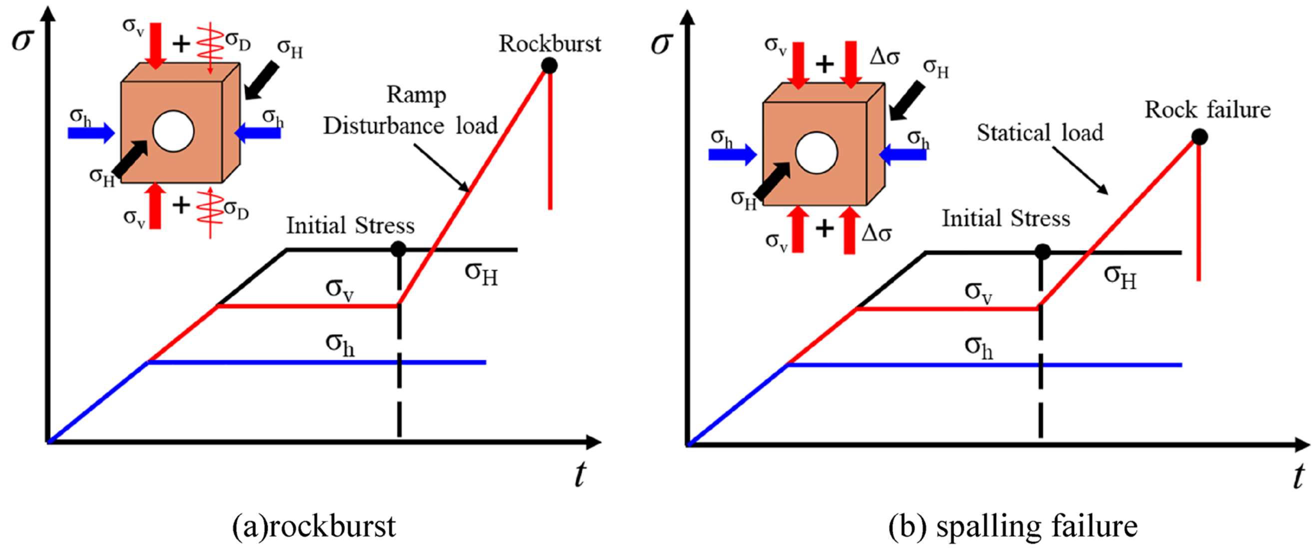

Fig. 6 Schematic of loading path

rates of the forces were the same in all three directions (0.5 kN/s), the stress loading rate in the *X* direction was smaller than that in the *Y* and *Z* directions (the stress loading rate in the *X* direction was about 0.05 MPa/s, and in the *Y*, *Z* directions were 0.09 MPa/s). This implies that before the corresponding initial stress state was reached, the slope of the stress-loading curve in the *X* direction was smaller than that of the stress-loading curve in the *Y* and *Z* directions. It can be seen from Fig. 7a that stress rises sharply and reaches the peak value in a short time period due to ramp dynamic disturbance. The duration of dynamic disturbance lasted less than 3 s. However, since the spalling failure was caused by static loading, the whole loading process took around 350 s, as evident in Fig. 7b.

3.2 Failure Process of the Hole Sidewalls

A miniature camera was equipped to record the failure process of the circular hole during the experiment. The typical failure process of rockburst and spalling failure is shown in Figs. 8 and 9, respectively. Figure 8a marks the vertical stress at 13.6 MPa. Herein, the rock was in the initial stress state, and intact. No failure phenomenon was observed. The strain energy generated during the loading stage started accumulating within the surrounding rock, marking the rockburst incubation stage. When dynamic disturbance load was applied (i.e., $\sigma_v = 50.5$ MPa), the left sidewall began to experience initial damage, indicating that the stress concentration coefficient of the left sidewall was high. Small particle ejection was observed, but the ejection velocity was low. However, the right sidewall remained intact without damage, as shown in Fig. 8b. After 0.02 s, the vertical stress reached 52.3 MPa, and the second visible particle ejection was observed on the left sidewall (see Fig. 8c), with a significantly higher velocity than that observed in Fig. 8b. Formation of multiple rock slabs on the left side wall accompanied by sight bulging of the right sidewall was seen when σ_v reached 56.3 MPa, as shown in Fig. 8d. As the vertical stress continued to increase, gradual initiation of cracks happened on the left and right sidewalls, which further propagated and penetrated the rock. Rock slabs started to peel off from the left and right sidewalls, as shown in Fig. 8e–g. At 321.24 s, the vertical stress reached the maximum value (i.e., $\sigma_v = 68.9$ MPa), and a rockburst occurred. A large number of rock particles and rock fragments were propelled violently outwards from the left and right sidewalls, as shown in Fig. 8h. Based on the observation, the whole process of rockburst can be summarized into four stages: quiet period, particle ejection, rock slabbing, and rockburst.

Figure 9 shows the process of spalling failure. When the vertical stress reached 13.6 MPa in Fig. 9a, no visible damage was seen. As the vertical stress continued to increase, micro-cracks appeared on the right sidewall and developed continuously, which resulted in lamellar rock slabs breaking outward to the surface, as shown in Fig. 9b, c. When $\sigma_v = 61.0$ MPa, cracks began to appear on the left sidewall, while the rock slabs on the right sidewall continued to develop and curl off towards the surface, resulting in small grains ejection at a low speed, as shown in Fig. 9d. The cracks on the left sidewall developed and expanded over time. The degree of damage on the left and right sidewalls gradually increased. Bulging and peeling off of a large number of rock slabs continued, as shown in Fig. 9e–g. In Fig. 9h, evident characteristics of spalling failure were seen on the left and right sidewalls when $\sigma_v = 64.6$ MPa. Many layered rock slabs were formed on the left and right

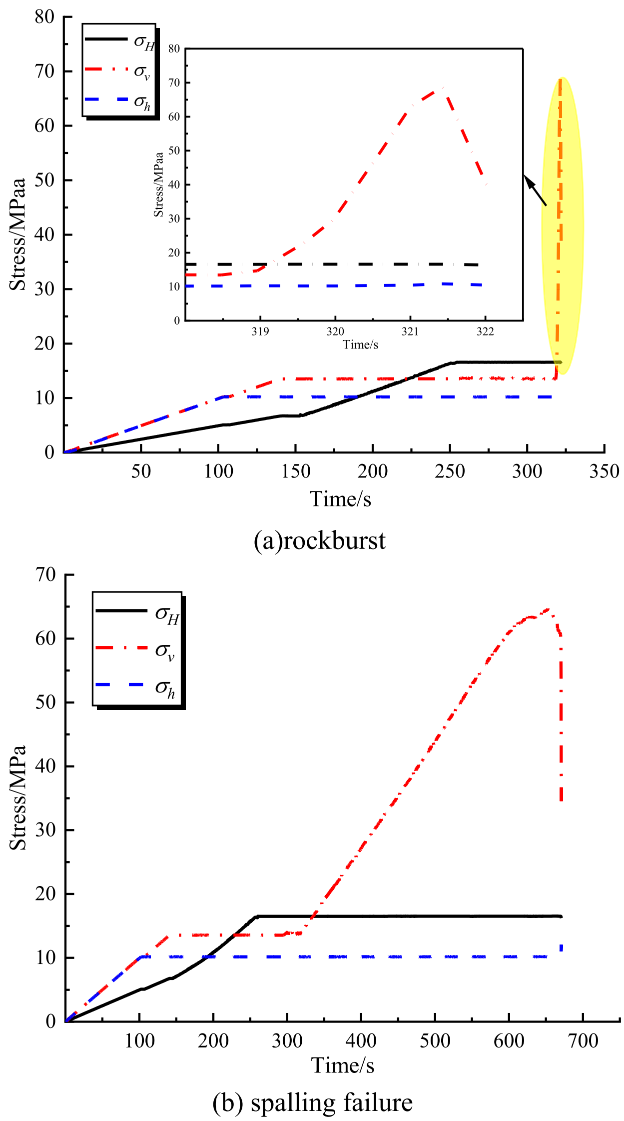

Fig. 7 Actual loading stress paths in true-triaxial tests

sidewalls, which constantly flaked off from the parent rock under the action of gravity. Thus, the spalling failure process can be divided into four stages during the test: quiet period, particle ejection, rock slabbing, and spalling failure.

Conclusively, it was found that spalling failure and rockburst shared three common stages, but their failure characteristics vary distinctly. The spalling failure was a slow static failure process, whereas, the rockburst was a dynamic failure process. The strain energy in the rock mass dissipated due to crack propagation and the remaining energy was converted into kinetic energy as rock fragments ejected during the rockburst. However, there is not enough remaining energy that gets converted into kinetic energy during the spalling failure.

4 Results Analysis

To further study the difference between rockburst and spalling failure, a detailed analysis was conducted considering four aspects of stress characteristics, AE characteristics, fragment characteristics, and morphology characteristics of *V*-shaped notch based on simulation experimental results.

4.1 Stress Characteristics

The surrounding rock before failure is assumed to be a homogeneous, continuous, and isotropic elastic body that does not deform along the axial direction of the tunnel (i.e., it is regarded as a plane strain problem). According to the elastic mechanic's theory, the maximum tangential stress can be obtained:

$$\sigma_{\theta\max} = 3p - q \tag{2}$$

where p and q are vertical stress and average horizontal stress, respectively. Let $p=\sigma_{\mathrm{v}}$ and $q=\sigma_{\mathrm{h}}$. Then the maximum tangential stress can be expressed as,

$$\sigma_{\theta\max} = 3\sigma_{\mathrm{v}} - \sigma_{\mathrm{h}} \tag{3}$$

The corresponding stress values σ_{v} and σ_{h} are obtained for the sidewall initial damage of spalling failure and rockburst by the visual analysis of the video of the sidewall damage recorded during the test. Substituting σ_{v} and σ_{h} into Eq. (3), the maximum tangential stress ($\sigma_{\theta\max}$) required for sidewall initial failure is obtained. Table 1 lists the *Y* direction stress values of initial sidewall failure (σ_{zi}) and $\sigma_{\theta\max}$.

It can be seen from Table 1 that the final failure stress of rockburst and spalling failure are 68.1 MPa and 62.9 MPa, respectively. The experimental results are consistent with the findings of Zhao (2000), which confirms that the dynamic strength of rock failure is higher than the static strength. Furthermore, the ratio of the maximum tangential stress to the uniaxial compressive strength of rockburst and spalling failure are 1.61 and 1.82, respectively. These results agree well with those of Gong et al. (2018) and Hu et al. (2019). This implies that compared with static load, the initial failure of surrounding rock under dynamic disturbance load requires less stress, that is, the initial failure of surrounding rock under dynamic disturbance load occurs sooner than that under static load. This is due to the fact that a high quantity of strain energy accumulates on the left and right sidewalls in a short period of time when a dynamic disturbance load is applied. When the accumulated strain energy exceeds the energy required for rock mass to fail, the strain energy is abruptly released from small areas on both sides of the hole. Spalling failure, on the other hand, is a slow and progressive failure process. In the case of spalling, the strain energy slowly accumulates

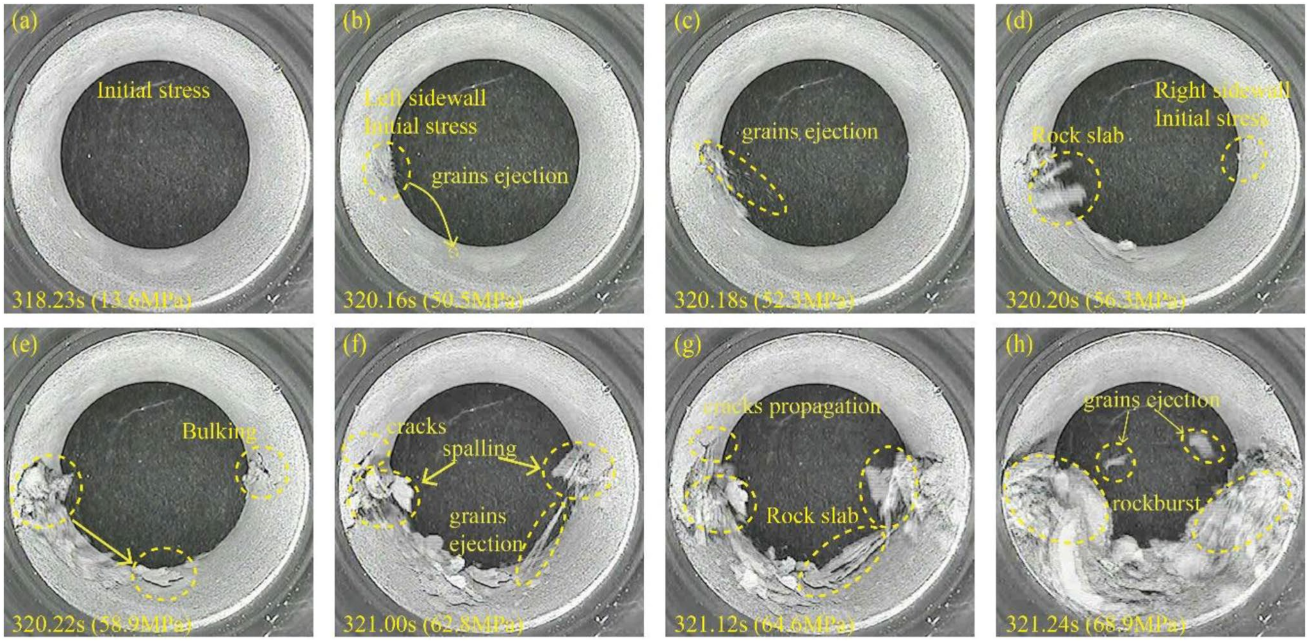

Fig. 8 Failure process of rockburst

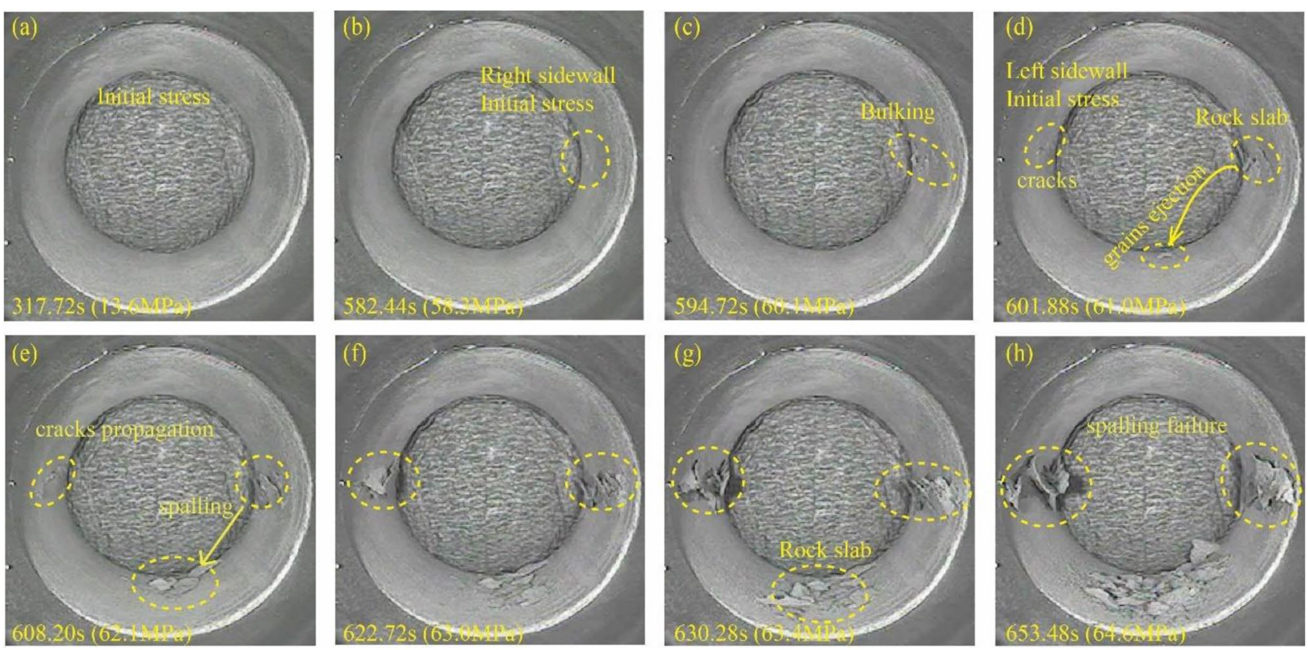

Fig. 9 Failure process of spalling failure

in the rock mass, and its distribution around the holes is relatively uniform. As a result, the strain energy accumulating in the surrounding rock takes longer to achieve the strain energy required for failure.

4.2 AE Characteristics

The process can be classified into three stages based on the stress path: stage I is the initial stress loading stage, stage II is the stress holding stage, and stage III is the dynamic disturbance load stage or static load stage. Stage I can be subdivided into three sub-stages. Stage I_1 represents the three-way

Table 1 Stress characteristics of sidewall initial fracture

	Specimen no.	Final stress (MPa)		σ_{zi} (MPa)	$\sigma_{\theta\max}$ (MPa)	$\sigma_{\theta\max}/\sigma_c$	
Rockburst	D1	68.9	68.1	50.5	141.3	1.62	1.61
	D2	71.1		49.4	137.2	1.58	
	D3	64.4		50.7	141.9	1.63	
Spalling failure	S1	64.6	62.9	58.3	164.7	1.89	1.82
	S2	60.5		54.4	153.0	1.76	
	S3	63.6		55.6	156.6	1.80	

synchronous loading stage, stage I_2 represents the two-way synchronous loading stage, and stage I_3 represents the one-way loading stage.

Amplitude and peak frequency are the main parameters of AE characteristics and reflect the rich information on rock fracture. Figures 10 and 11 show the relationship between the amplitude and peak frequency of rockburst and spalling failure, respectively. As can be seen from Figs. 10 and 11, AE amplitude ranges from 40 to 100 dB and peak frequency ranges from 0 to 400 kHz. According to the experimental results, the amplitude can be divided into five groups: low amplitude (40–60 dB), middle amplitude (60–70 dB), middle and high amplitude (70–80 dB), high amplitude (80–90 dB), and ultra-high amplitude (90–100 dB). Similarly, the corresponding peak frequencies can be divided into four groups: low frequency (0–100 kHz), middle frequency (100–200 kHz), high frequency (200–350 kHz), and ultra-high frequency (350–400 kHz).

During stage I_1, the rock is under triaxial compression and the internal primary cracks are closed, as seen in Figs. 10 and 11. The AE signals are active, and most AE signals are in the range of low amplitude, medium frequency, and high frequency. Stage I_2 and stage I_3 are two-way loading and one-way loading, respectively, compared with stage I_1. The number of AE is less, and their frequency distribution gradually shifts from middle frequency and high frequency to middle frequency. Stage II is the stress-holding stage, in which the AE signals are scattered, the AE activity is low, and no damage occurs inside the sample. During stage III as seen in Fig. 10, the vertical stress increases dramatically due to dynamic disturbance load, resulting in multiple cracks intersecting each other, and AE signal activity increases. During the period of dynamic disturbance load (i.e., stage III), AE signals (> 70 dB) are generated frequently and concentrated in the range of medium frequency. Moreover, the quiet period of AE can be observed clearly. Stage III in Fig. 11 corresponds to the static load stage. Due to the slow loading rate during stage III, there are many AE signals generated with low amplitude having a frequency in the range of 100–350 kHz. According to the enlarged picture in Fig. 11, the AE signals with low and medium amplitude (i.e., 40–70 dB) are generated during the spalling failure (to facilitate observation, 40–60 dB low amplitude signals are filtered in the local magnification). However, the quiet period of AE could not be observed during the spalling failure.

The characteristic parameters of AE are summarized in Table 2. The AE signal frequency of rockburst is distributed in the range of 100–200 kHz, while that of spalling failure is in the range of 100–350 kHz, indicating that the AE signal frequency of rockburst is lower than spalling failure. According to Cai et al. (2007b), the high frequency of the AE signal represents small-scale cracks and the low frequency represents large-scale cracks. Therefore, it can be inferred from the results that rockburst is mainly caused by large-scale cracks, while spalling failure is mainly caused by small-scale cracks. And the damage from rockburst, due to large-scale cracks, is more severe. In addition to this, the percentage of AE signals larger than 70 dB generated during rockburst is more than 70%, and the cumulative AE energy is as high as 4.64×10^8 aJ, while the percentage of AE signals larger than 70 dB generated by spalling failure is less than 1%, and the cumulative AE energy is only 0.32×10^8 aJ. With respect to the AE energy aspect, it can be said that rockburst is more severe than spalling failure. It is worth noting that the quiet period of AE can be observed during the rockburst, but there is no quiet period in spalling failure. This phenomenon is mainly due to the fact that rockburst is caused by large-scale cracks, which hinder the propagation of elastic waves generated by micro-cracks in the rock, resulting in only AE signals with high amplitude being received.

The relationship between average frequency (AF) and RA (the ratio of rise time to amplitude) can further be used to classify micro-cracks in rocks (Ohno and Ohtsu 2010). Figure 12 shows the schematic illustration of the method to classify microcracks based on the scatters of AF–RA. A boundary line with slope k (AF/RA) is used to distinguish shear and tensile cracks, assuming k is equal to 1.2 (Wang et al. 2019a). Figures 13 and 14 show the kernel density of AF and RA at different stages of rockburst and spalling failure, and Fig. 15 shows the proportional change of shear (tensile) cracks. From Fig. 13 it can be seen that due to the closure of primary cracks, a large number of AE signals are generated in stage I_1, which are

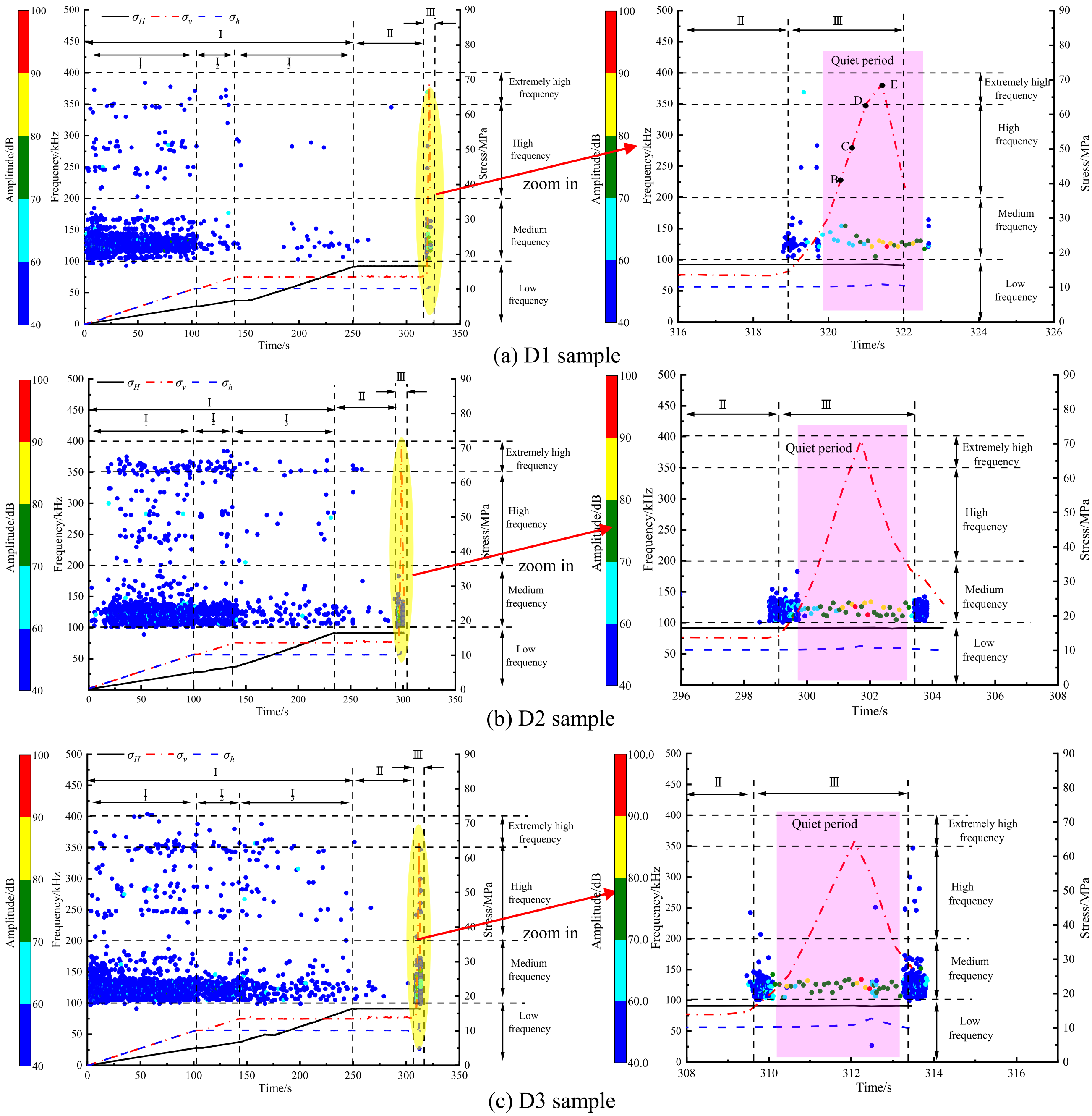

Fig. 10 The amplitude-frequency characteristic curves of rockburst

concentrated in the tension region. With the increase of stress, AE signals generated in I_2 and I_3 stages are less, but tensile cracks are still dominant. It can be seen from Fig. 15a that the proportion of tensile cracks in stages I_1, I_2 and I_3 of rockburst is greater than 60%, which is much larger than the proportion of shear cracks. In stage III, the concentrated area of AE gradually shifts from the tension region to the shear region, indicating that shear cracks are dominant during rockburst, however, a large number of tensile cracks are still present (shear cracks account for 58% and tensile cracks account for 42%). Figure 14 shows that AE signals are always concentrated in the tension region during spalling failure, and in stage III, tensile failure is dominant (70% tensile crack and 30% shear crack). It can be inferred from the above observations that the mechanism of rockburst is complex, which includes coupling of tension-shear cracks, while the mechanism of spalling failure is simple, including only tensile cracks.

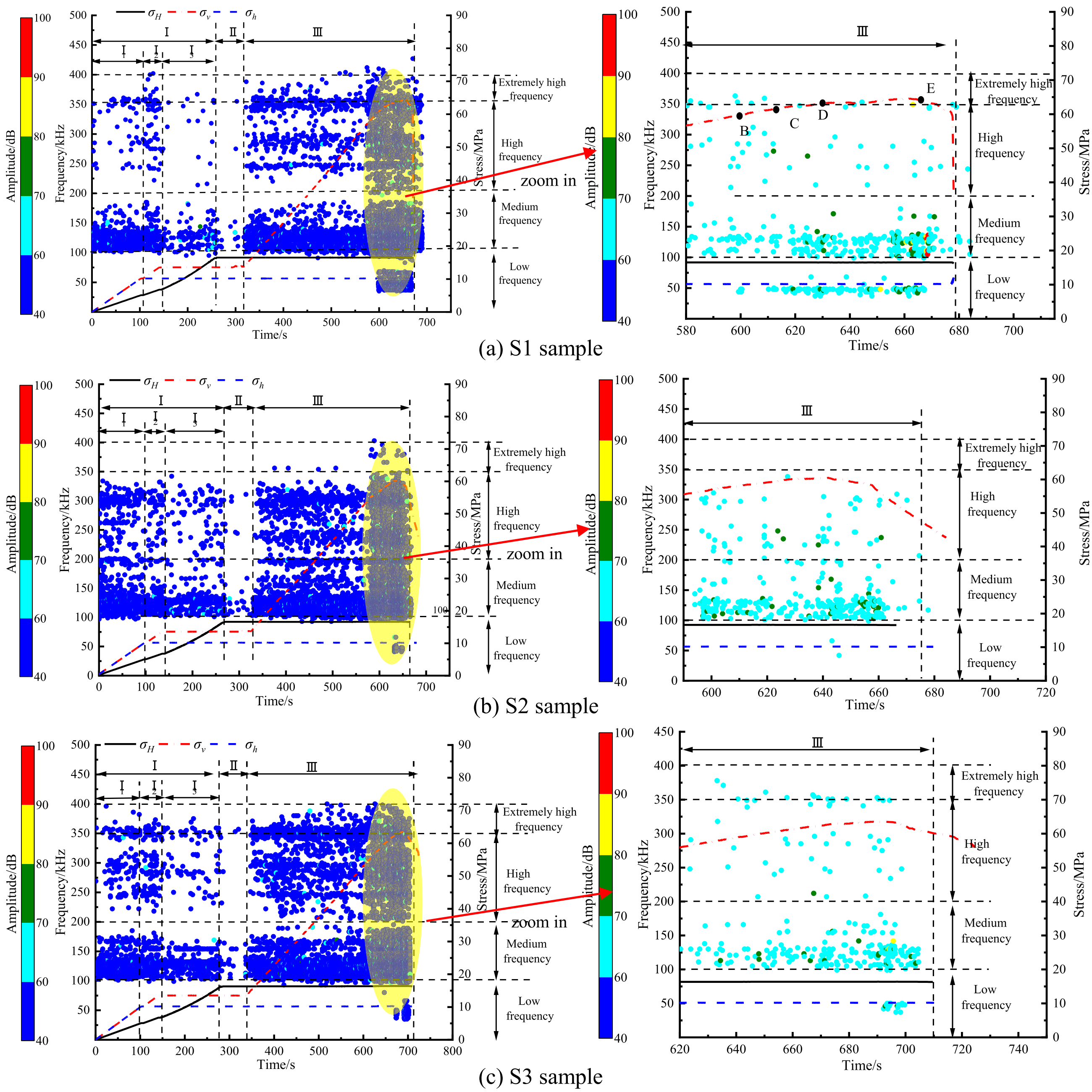

Fig. 11 The amplitude-frequency characteristic curves of spalling failure

4.3 Fragments Characteristics

After the experiment, rock fragments were collected, screened, and measured. Figures 16 and 17 show the fragments of rockburst and spalling failure, respectively. It can be seen from Figs. 16 and 17, that the amount of fragments of rockburst is much more than that of spalling failure. Furthermore, the morphological characteristics of fragments differ, with rockburst fragments being in long strips and spalling failure fragments being as flakes or plates. Figure 18 and Table 3 present the number of fragments and the ratio of width to length of fragments. Average number of fragments generated in rockburst is 39, which is far more than the number of fragments generated by spalling failure,

Table 2 Characteristic parameter of acoustic emission (AE)

	Specimen no.	Frequency (kHz)	Ratio* (%)		Cumulative energy (10^8 aJ)		Quiet period
Rockburst	D1	100–200	73.1	74.8	6.51	4.64	√
	D2		80.0		3.02		√
	D3		71.3		4.35		√
Spalling failure	S1	100–350	0.11	0.12	0.57	0.32	×
	S2		0.08		0.23		×
	S3		0.16		0.15		×

Ratio represents that the ratio of AE signal larger than 70 dB to total AE signal during stage III; "√" represents that the quiet period of AE exists during stage III; "×" represents that the quiet period of AE does not exist during stage III

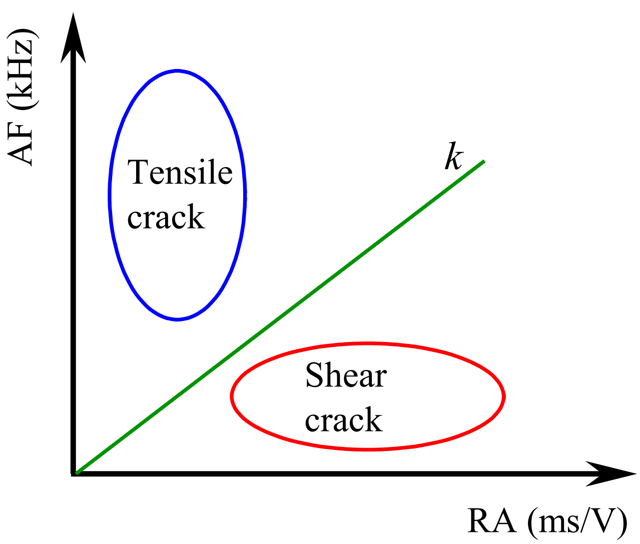

Fig. 12 Schematic of crack type classification by AF and RA values

indicating that the energy released by rockburst is greater than that released by spalling failure. Moreover, the average ratio of width to length of fragments in rockburst and spalling failure is 0.58 and 0.63, respectively, which proves that the rockburst is more violent than spalling failure.

Fractal theory can be used to quantitatively describe various complex morphologies of different materials' surfaces. Rock failure goes through the process of crack initiation, propagation, and penetration, during which a lot of energy is dissipated. Previous studies have demonstrated that the rock fragments possess the property of statistical self-similarity and the fractal dimension of fragments can reflect the severity of rock failure and energy consumption. The fractal dimension can be calculated in form of granularity–quantity, perimeter–quantity, and area–quantity by using the area, perimeter, length, and width of fragments.

The area of fragments is converted into equivalent side length L_{eq}, and the fractal dimension of granularity–quantity is expressed as:

$$\begin{cases} N = N_0 \left(L_{\text{eq}} / L_{\text{eqmax}} \right)^{-D} \\ L_{\text{eq}} = \sqrt[2]{l \times w} \end{cases} \tag{4}$$

where N is the number of fragments whose equivalent side length is greater than L_{eq}, N_0 is the number of fragments whose equivalent side length is L_{eqmax} ($N_0 = 1$), D is the fractal dimension, w and l are width and length of fragments, respectively. The logarithmic relationship between L_{eqmax}/L_{eq} and N/N_0 is shown in Fig. 19a. The absolute value of the slope of the linear fitting curve in Fig. 19a is the fractal dimension of granularity–quantity. The fractal dimension of perimeter–quantity and area–quantity can be calculated using a similar method.

The fractal dimensions are summarized in Table 4 and Fig. 19. For rockburst, the average fractal dimensions of granularity–quantity, perimeter–quantity, and area–quantity are 2.43, 2.15, and 1.35, respectively. For spalling failure, the average fractal dimensions of granularity–quantity, perimeter–quantity, and area–quantity are 2.41, 2.12, and 1.33, respectively. Although fractal dimensions obtained by different calculation methods are different, in general, the fractal dimensions of spalling failure are smaller than those of rockburst. The fractal dimension reflects the severity of rock failure. The larger the fractal dimension, the more violent rock failure. Therefore, the results further indicate that the rockburst is more violent than spalling failure.

4.4 Morphology Characteristics of *V*-shaped Notch

Figures 20 and 21 show the overall and local damage suffered by the samples after rockburst and spalling failure. It can be seen that rockburst and spalling failure occurred on both sidewalls of the hole, along with the formation of *V*-shaped notches. However, there is a large difference in the morphology characteristics of *V*-shaped notches between rockburst and spalling failure. Rock samples of rockburst experience violent damage which is in contrast to the spalling failure. A lot of tensile cracks can be observed around the middle of the hole, and two dominant shear

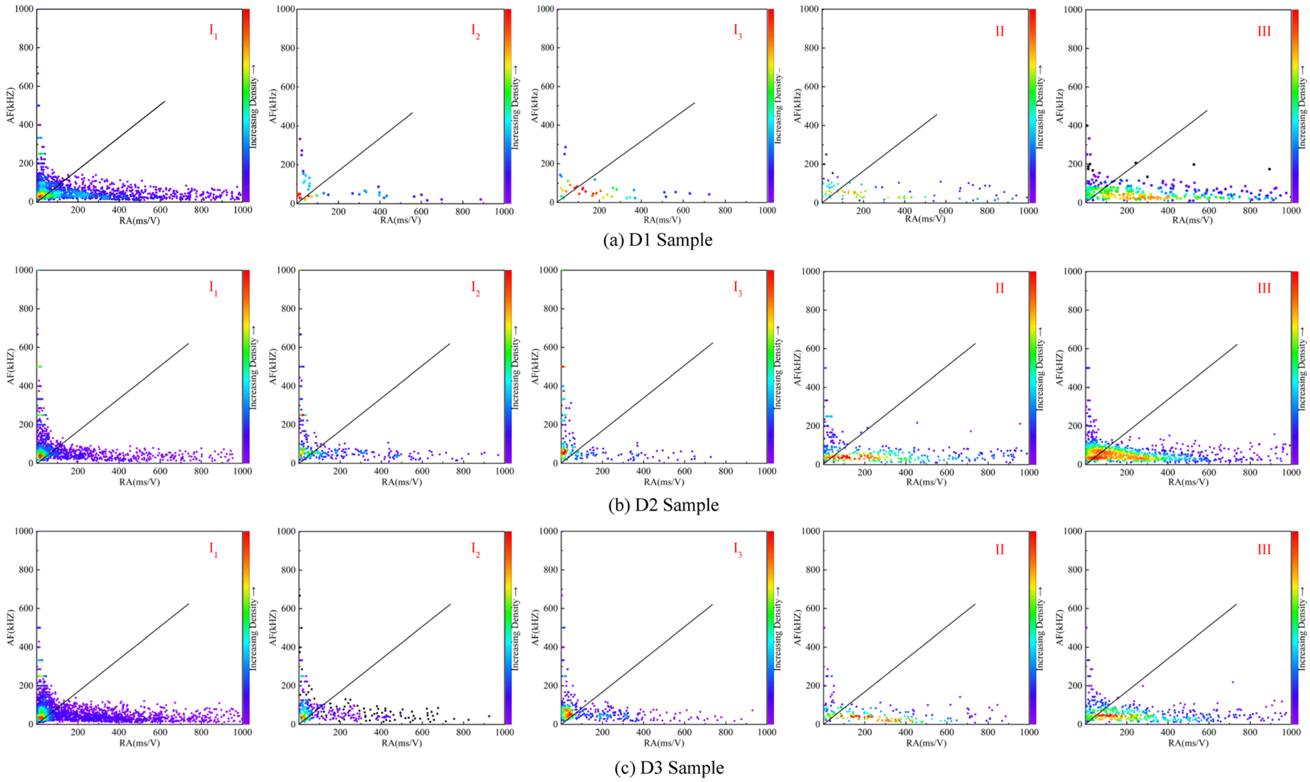

Fig. 13 Kernel density of AF and RA of rockburst

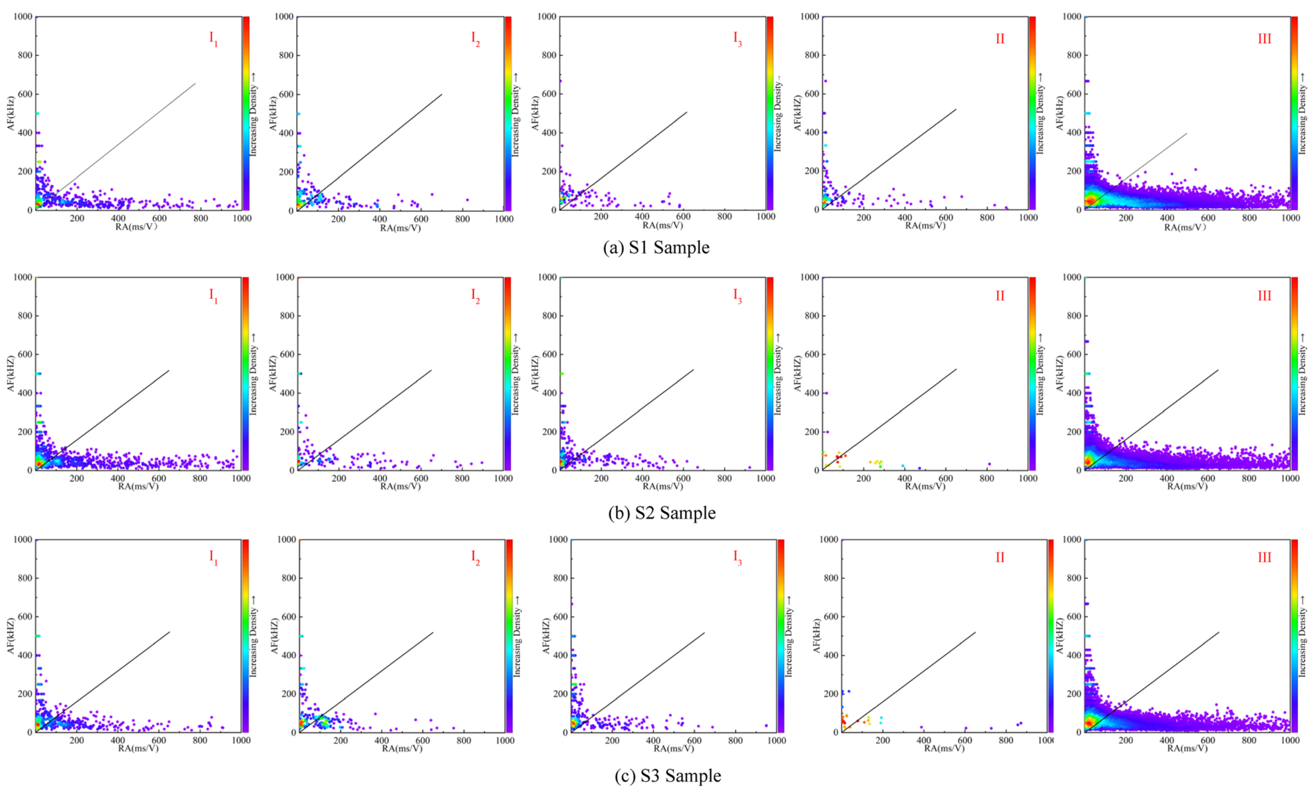

Fig. 14 Kernel density of AF and RA of spalling failure

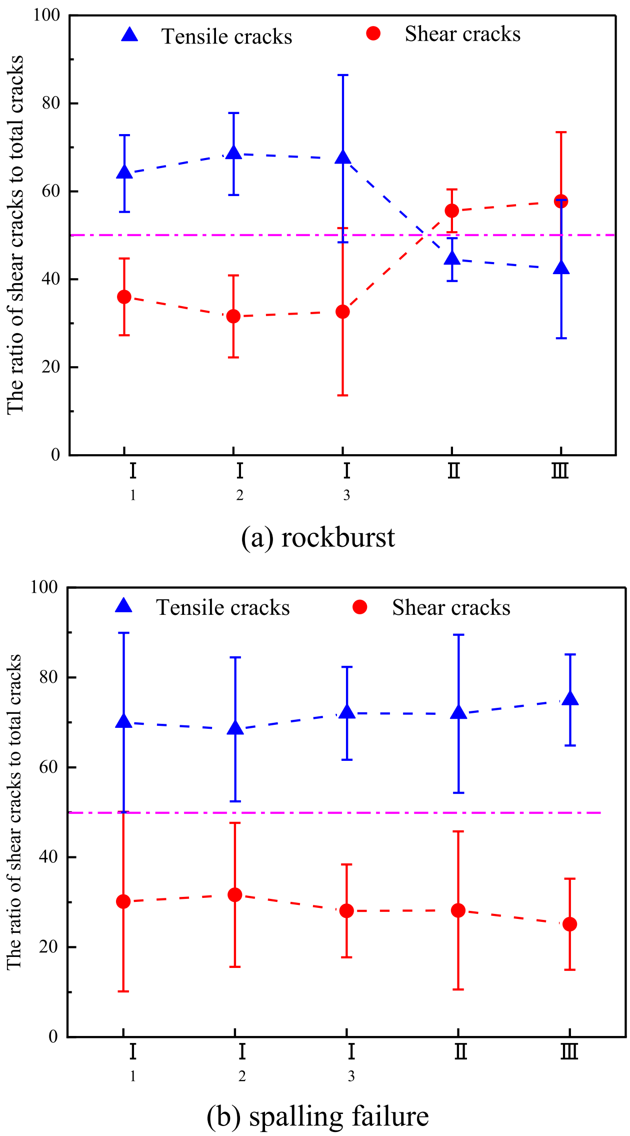

Fig. 15 The ratio of shear (tensile) cracks to total cracks

cracks can be seen along the diagonal of the rock samples (see Fig. 20). Whereas, rock samples of spalling failure are intact and just a few tensile cracks can be seen in the *V*-shaped notches (see Fig. 21). Therefore, the rockburst is characterized by shear-tensile failure, whereas the spalling failure is characterized by tensile failure. Furthermore, both the rockburst and the spalling failure produce multilayer rock slabs, demonstrating that the rockburst and spalling failure evolve layer by layer from the surface of the tunnel to the deep surrounding rock. The *V*-shaped notches boundary of rockburst is jagged, which is more complex than the spalling failure, whereas the *V*-shaped notches boundary of spalling failure is parallel to the axis of the hole. Figure 22 shows the failure mode of the tunnel in the engineering site, which is consistent with the experimental result presented in Figs. 20 and 21. This indicates that the experimental result in this paper is reliable and effective to simulate the rockburst and spalling failure.

The rock sample photos are imported into the image processing software, and the outline is sketched with smooth curves, as shown in Fig. 23. The depth and angle of *V*-shaped notches are calculated as suggested by Wang et al. (2019a) (see Fig. 24) and are presented in Table 5 and Fig. 25. The result shows that the average angles of the left and right *V*-shaped notch of rockburst are 84.3° and 89.7°, respectively, and the average depths are 5.12 mm and 6.62 mm, respectively. Whereas, the average angles of the left and right *V*-shaped notch of spalling failure are 102.3° and 103.7°, and the average depths are 2.78 mm and 3.23 mm, respectively. In contrast, *V*-shaped notches of rockburst are narrow and deep, while *V*-shaped notches of spalling failure are wide and shallow, which demonstrates that the damage scope of rockburst is smaller, and energy is released in a small area, leading to the violent ejection of rock fragments. However, the damage scope of spalling failure is large, and the energy is gradually released in a large area. The energy release is relatively slow, and there is no fragment ejection with high speed. It should be noted

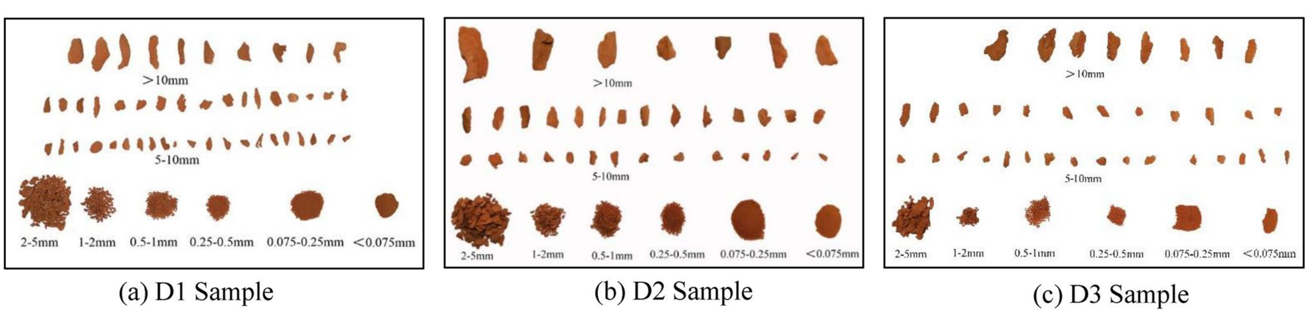

Fig. 16 Classification of fragments of rockburst

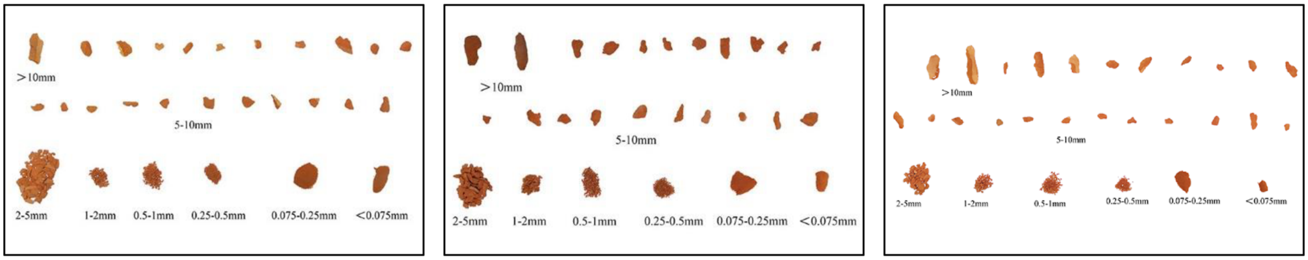

(a) S1 Sample (b) S2 Sample (c) S3 Sample

Fig. 17 Classification of fragments of spalling failure

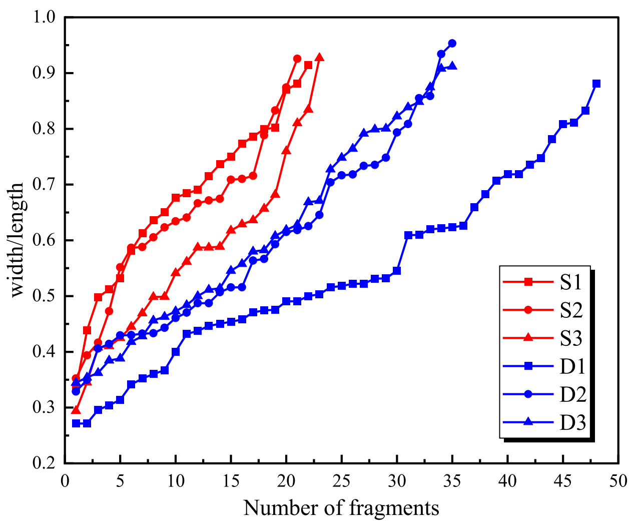

Fig. 18 Characteristics of width-to-length ratio

Table 3 Number of fragments and characteristics of width-to-length ratio

	Specimen no.	The number of fragments		The ratio of width to length	
Rockburst	D1	48	39	0.27–0.88	0.58
	D2	35		0.33–0.95	
	D3	35		0.34–0.91	
Spalling failure	S1	22	22	0.34–0.92	0.63
	S2	21		0.35–0.93	
	S3	23		0.30–0.93	

that the angles and depths on both sidewalls should be symmetrically distributed, however, the experimental results do not show the feature of symmetrical distribution, which may be caused by the heterogeneity of the rock.

5 Discussion

5.1 Influence of Scale Effect

The scale effect is a common concern in the experimental studies of rock mechanical properties in the laboratory. Generally, to satisfy 3–5 times the excavation radius, a large-scale physical model experiment is usually used (seen Fig. 26). Furthermore, the experimental sample was made using similar materials, such as gypsum and concrete, which although have similar mechanical behavior, are different from the rock material. Reproducing the rockburst process is a challenging task. If a large-scale rock block is used to simulate a rockburst, two primary problems will encounter. One is the difficulty of sampling on site, and the other is the high requirement of the loading capacity of the experimental machine. Therefore, some scholars, such as (i) Gong et al. (2018); (ii) Luo et al. (2020); (iii) Wang et al. (2019b) employed small-scale rock samples with a circular hole in the center to simulate rockburst (seen Fig. 27). In addition, Martin (1997) conducted compression test on granite with different hole diameters. The result shows that the ratio of tangential stress to uniaxial compression strength will increase sharply when the hole diameters are less than 50 mm, which will result in an inaccurate experiment result. Based on the above reason, in this study, a circular hole with 50 mm diameters was adopted in the experimental tests considering the available testing conditions. Though the size of rock specimens used in this paper cannot satisfy 3–5 times the excavation radius, the experiment result can help enhance the understanding of rockburst and spalling failure.

5.2 Influence of Loading Mode on Failure Process

Figure 28 is a schematic diagram showing the evolution of rock failure of rockburst and spalling failure. As mentioned in Sect. 3.2, the failure process of rockburst and spalling failure can be divided into four stages, i.e., quiet period, particle ejection period, rock slabbing period, and rockburst

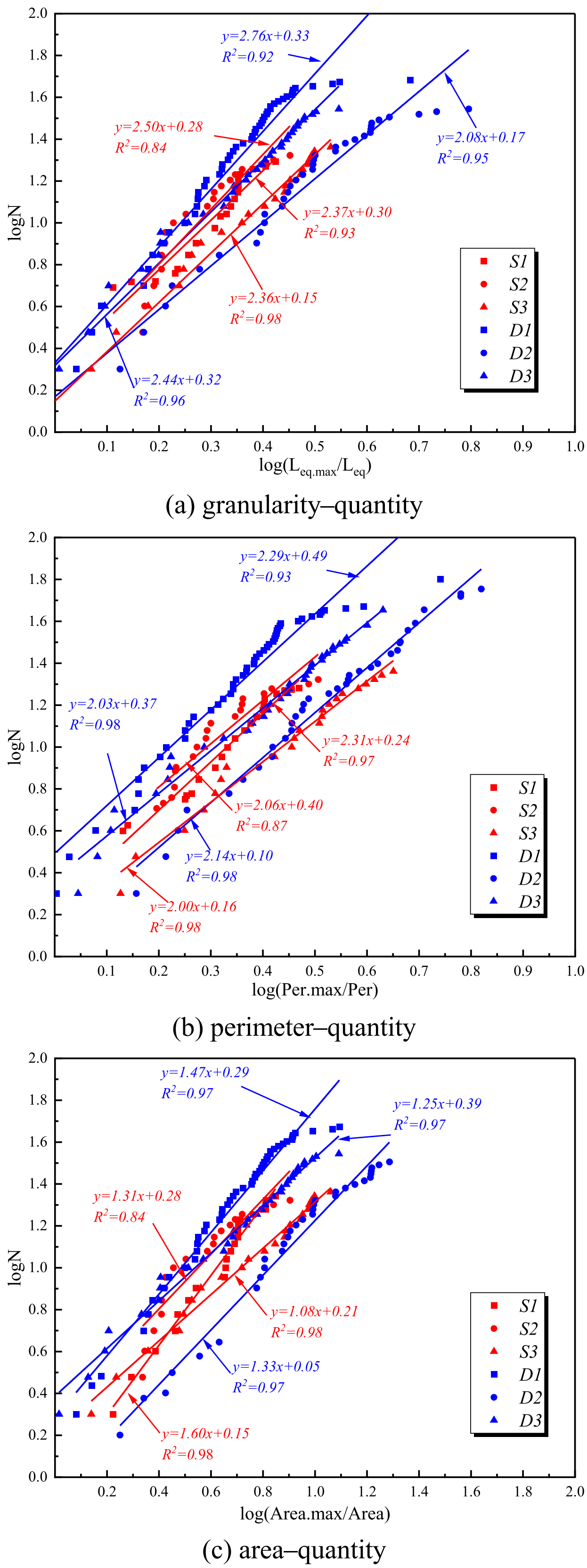

Fig. 19 Characteristics of fractal dimension

or spalling failure period. The characteristics of each stage can be stated as follows:

1. The quiet period: The tangential stress reaches $\sigma_{\theta 1}$. No macroscopic damage can be seen on the sidewall, but micro-cracks have begun to propagate in the surrounding rock (see Fig. 28a).
2. The particle ejection period: During this period, no visible buckling deformation appears on the sidewall and the tensile crack propagates along the direction of the tangential stress. The tangential stress reaches $\sigma_{\theta 2}$ and particle ejection from the center of the sidewalls initiates (see Fig. 28b). This demonstrates that some micro-cracks have intersected each other on the sidewall, but there is no visible accumulation of fragments in the bottom of the hole because the ejected particles are small.
3. The rock slabbing period: As the tangential stress reaches $\sigma_{\theta 3}$, the sidewall begins to deform and the rock near the surface splits into small rock plates, which continuously open outward (see Fig. 28c). A large number of micro-cracks intersect and coalesce to form a larger-scale crack, and visible rock slabbing occurs.
4. The rockburst or spalling failure period: The tangential stress reaches ($\sigma_{\theta 3} + \Delta 1$), buckled rock plates instantaneously fracture and separate from the sidewall, triggering the rockburst. The elastic energy stored in these rock plates is suddenly released, part of the energy converts into dissipative energy by rock breaking, and part of the energy converts into the ejection kinetic energy of fragments, resulting in rock fragments being thrown into the hole space at high speed (see Fig. 28d). However, when the tangential stress reaches ($\sigma_{\theta 3} + \Delta 2$) (noting that the $\Delta 2$ is less than $\Delta 1$), the spalling damage is further evolved, and the tensile crack gradually propagates toward the inside of the sidewall. Multiple cracks propagate and penetrate simultaneously, resulting in the frizzy rock plates to continuously open and slip from the sidewalls with no abrupt ejection (see Fig. 28e).

It can be inferred that if the tangential stress is increasing when the spalling failure occurs, i.e., $\Delta 2$ comes closer to $\Delta 1$ gradually, a rockburst will occur accompanied by violent ejection of rock fragments. Previous studies have shown that spalling failure is an inevitable and precursor phenomenon for rockburst in intact rocks around deep tunnels (He et al. 2010; Gong et al. 2019). Historically, spalling failure has often been used as an indicator to provide a warning for rockburst. However, it should be noted that spalling failure does not imply that the occurrence of rockburst is inevitable. Although every rockburst is accompanied by spalling failures.

Comparison of rockburst and spalling failure at $\sigma_v = 55$ MPa and $\sigma_v = 60$ MPa, as presented in Fig. 29, has

Table 4 Fractal dimensions of fragments

	Specimen no.	Granularity–quantity		Perimeter–quantity		Area–quantity	
		D	Average	*D*	Average	*D*	Average
Rockburst	D1	2.76	2.43	2.29	2.15	1.47	1.35
	D2	2.08		2.14		1.33	
	D3	2.44		2.03		1.25	
Spalling failure	S1	2.37	2.41	2.31	2.12	1.60	1.33
	S2	2.50		2.06		1.31	
	S3	2.36		2.00		1.08	

been done to study the failure characteristics of surrounding rock under static load and dynamic disturbance load. When $\sigma_v = 55$ MPa, a visible failure phenomenon occurs on the left sidewall with a large number of rock fragments peeling off from the parent rock, while the right sidewall remains intact (see Fig. 29a). Compared with rockburst, the severity of spalling failure is significantly less when $\sigma_v = 55$ MPa. There is no apparent failure on either of the sidewalls, however, a small bulging of rock slabs on the right sidewall is seen in Fig. 29b.

When $\sigma_v = 60$ MPa, both sidewalls are damaged severely, a large number of rock fragments buckle and bulge steadily, and even some rock fragments are ejected at a high speed (see Fig. 29a). However, for spalling failure, although the left and right sidewalls are similarly damaged to a large extent when $\sigma_v = 60$ MPa, with multiple layered rock fragmentation, no ejection of fragments happens. The rock fragments only slide slowly under the action of gravity. Therefore, the severity of spalling failure is slight than rockburst.

This indicates that the failure of surrounding rock under dynamic disturbance load is more apparent than spalling failure under the same vertical stress, and high-speed rock fragment ejection is more likely to occur. Therefore, in deep underground rock engineering, it is necessary to avoid the generation of dynamic disturbance load or reduce the rate of dynamic disturbance load.

5.3 Strain Energy of the Surrounding Rock

Rock masses can store a large amount of strain energy under high-stress conditions. Once the stored strain energy exceeds the strain energy required for rock failure, the strain energy inside the rock releases quickly, resulting in serious disasters. Before the onset of rock failure, it is assumed that the rock element is a continuous and uniform elastic body. The elastic strain energy in the rock can be calculated according to the Eq. (5)

$$\begin{cases} W = \int F_X \mathrm{d}L_X + \int F_Y \mathrm{d}L_Y + \int F_Z \mathrm{d}L_Z \\ V_\varepsilon = \frac{W}{V} \end{cases} \quad (5)$$

where W is the strain energy, i.e., the work done by external force; F_X, F_Y, F_Z and L_X, L_Y, L_Z are the forces and displacements in the direction of X, Y, Z, respectively; V is the rock specimen volume ($V = 5.07 \times 10^{-4}$ m^3); and V_ε is the strain energy density.

The forces and displacements in the X, Y, and Z directions were measured when the rockburst or spalling failure occurred. The strain energy in all three directions and the strain energy density of the specimen was calculated. The results are summarized in Table 6. The result in Table 6 shows that the average strain energy density of rockburst is 798.80 kJ/m^3, and that of spalling failure is 739.13 kJ/m^3. The strain energy released by the surrounding rock of the roadway under dynamic disturbance load is higher than that released under static load, thus the severity of rockburst is higher than spalling failure as well, which is consistent with the previous research conclusions.

Rockburst or spalling failure will happen only when the strain energy accumulated in the rocks exceeds the energy that is necessary for rock failure, and there is enough excess energy (ΔE) that can be released in the form of kinetic energy or other forms. In the uniaxial compression test, it is assumed that the critical maximum principal strain before the rockburst or spalling failure is equal to the axial strain at the peak stress. The excess energy stored in the sample is mainly released, which induces the rockburst or spalling failure (He et al. 2012). The energy calculation model is shown in Fig. 30.

The mechanism of the rockburst and spalling failure can be analyzed according to the failure process discusses in Sect. 5.2, from the viewpoint of energy, as illustrated in Fig. 31.

Firstly, it is assumed that the required energy for rock failure under the uniaxial compression test is E_0.

Secondly, significant elastic strain energy is stored in the surrounding rocks during the quiet period of rockburst and spalling failure. Since the stress is less than the strength of the rocks, the stored strain energy E_1' and E_2' is lower than E_0 (E_1' and E_2' are stored strain energy during the quiet period of rockburst and spalling failure, respectively).

Thirdly, both sidewalls begin to exhibit initial failure in both rockburst and spalling failure after the quiet period, i.e.,

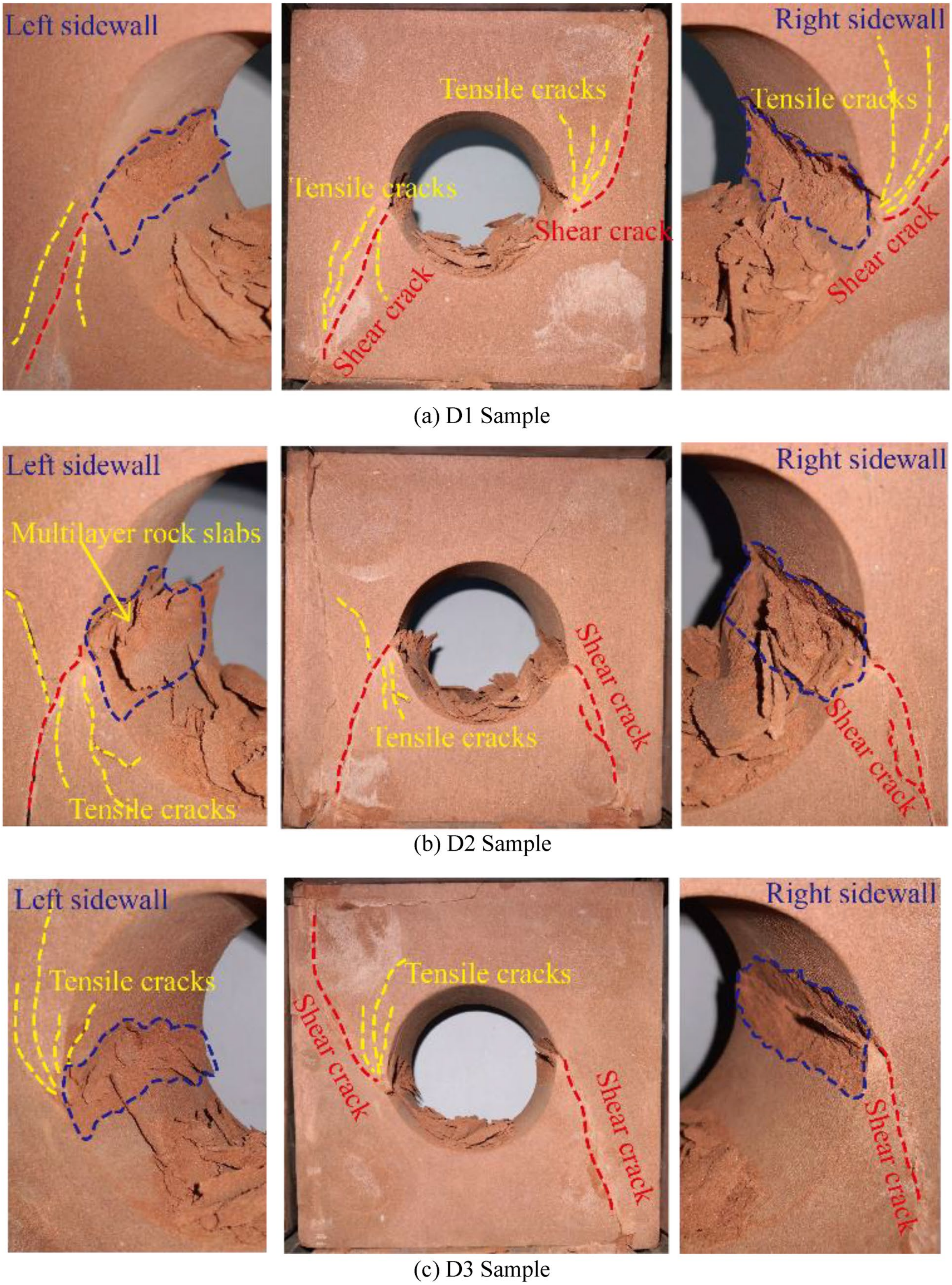

Fig. 20 Photos of specimens after rockburst

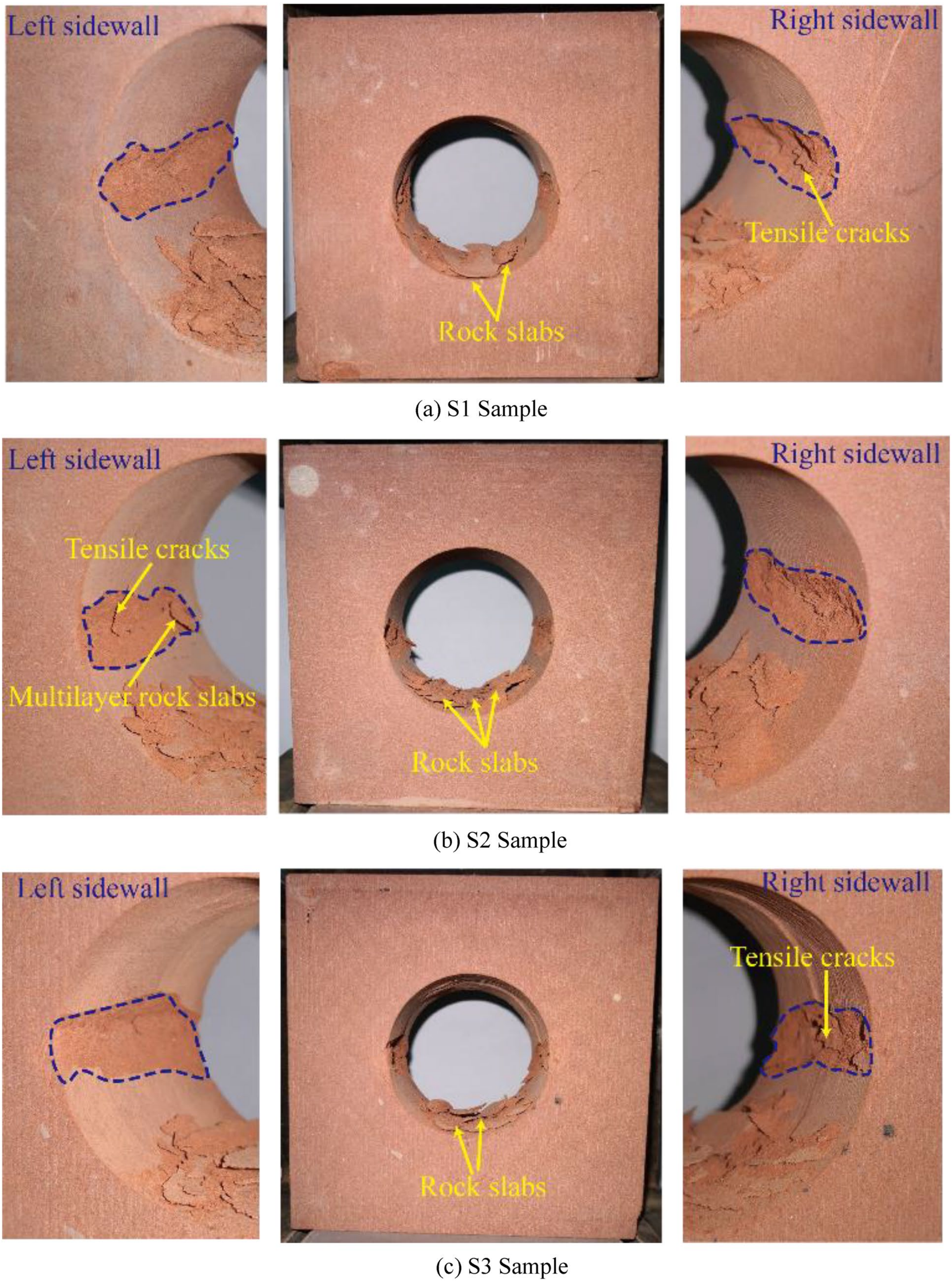

Fig. 21 Photos of specimens after spalling failure

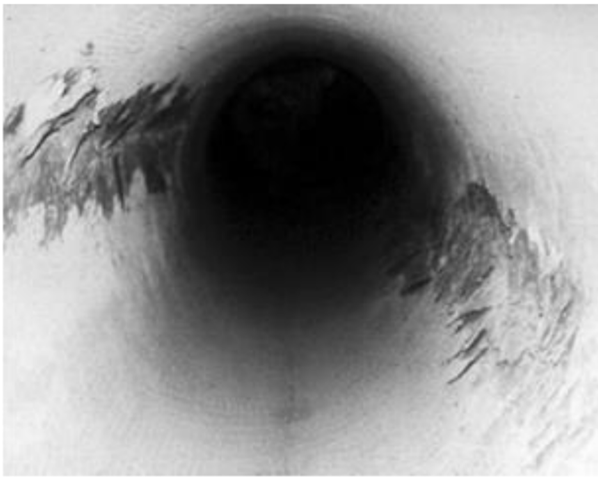

(a) V-shaped notch in the tunnel (Hoke 2014)

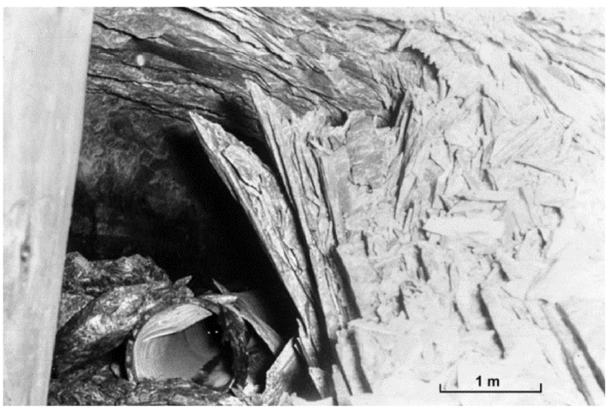

(b) severe rock failure in an access tunnel (Hoke 2014)

Fig. 22 On-site failure model of surrounding rock

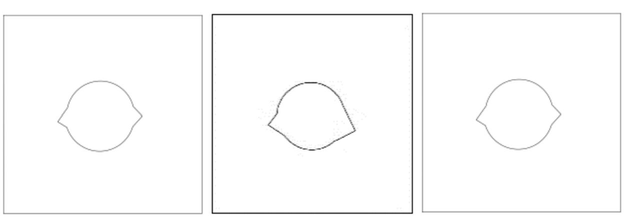

(a) rockburst

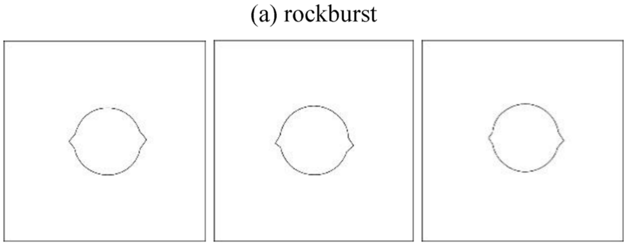

(b) spalling failure

Fig. 23 Schematic diagram of *V*-shaped

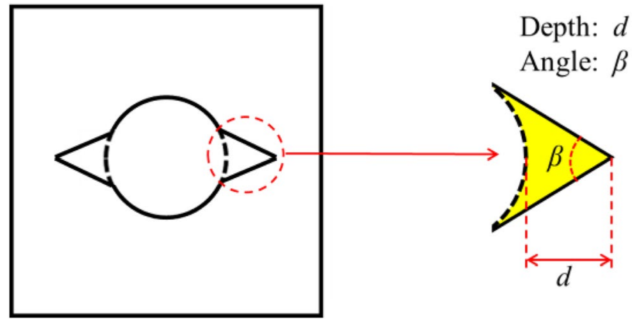

Fig. 24 Schematic diagram of *V*-shaped notch

the stored strain energy E_1'' and E_2'' is higher than E_0 (E_1'' and E_2'' are stored strain energy of rockburst and spalling failure when the initial failure occurred, respectively). However, E_1'' and E_2'' is not large enough to cause violent particle ejection and excess energy is just dissipated by the cracks propagation and plastic deformation.

Finally, when the rockburst or spalling failure occurs, the stored strain energy E_1 and E_2 surpasses E_0, as shown in Fig. 31, resulting in serious failure on both left and right sidewalls. However, the excess energy ΔE_1 of spalling failure is lower than the excess energy ΔE_2 of a rockburst. This indicates that the excess energy ΔE_1 is all consumed by the cracks propagation, resulting in multiple rock plate exfoliation and no violent particle ejection. The excess energy ΔE_2 is consumed not only by the cracks propagation but also part of ΔE_2 is converted to kinetic energy, resulting in violent particle ejection.

6 Conclusions

Rockburst caused by the dynamic disturbance load and the spalling failure caused by the static load was investigated using a cubic red sandstone with a circular hole. Simultaneously, the AE signals and failure process was monitored and collected by the AE system and miniature camera. The experiment results were analyzed and discussed in detail. The main conclusions are as follows:

1. The evolution process of rockburst and spalling failure was reproduced. Rockburst failure was a dynamic phenomenon and usually occurred suddenly and violently. The process of rockburst could be divided into four stages: quiet period, particle ejection, rock slabbing, and rockburst. The spalling failure was a slow and progressive static failure, which included four stages: quiet period, particle ejection, rock slabbing, and spalling failure. Thus, spalling failure can be regarded as a precursor phenomenon of rockburst failure.

Table 5 Morphological characteristics of *V*-shaped notch

	Specimen no.	Angle (°)				Depth (mm)			
		Left	Average	Right	Average	Left	Average	Right	Average
Rockburst	D1	82	84.3	83	89.7	4.98	5.12	7.28	6.62
	D2	85		91		4.96		7.58	
	D3	86		95		5.42		5.00	
Spalling failure	S1	101	102.3	105	103.7	3.33	2.78	3.81	3.23
	S2	96		110		2.66		2.91	
	S3	110		106		2.35		2.97	

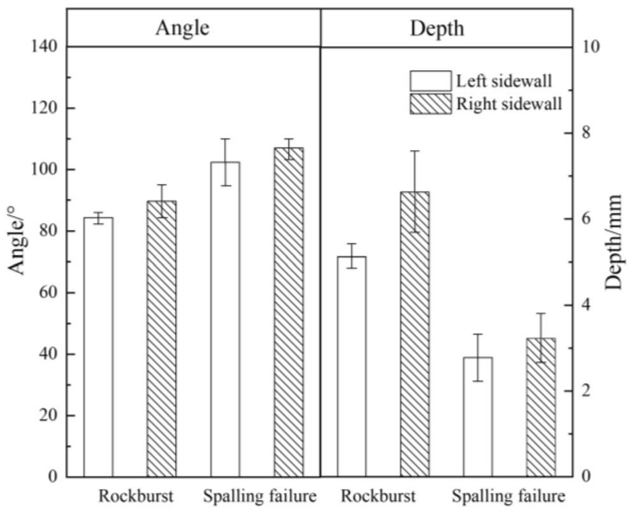

Fig. 25 Depth and angle of *V*-shaped notch

2. The final failure strength of the surrounding rock under dynamic disturbance load was higher than that under static load. However, under dynamic disturbance load, the initial failure stress of the surrounding rock was lower than that under static load, indicating that the surrounding rock was more prone to failure under dynamic disturbance load.
3. The AE signals with high amplitude generated during the rockburst were distributed in the range of 100–200 kHz. However, the AE signals of spalling failure were distributed in the range of 100–350 kHz, wherein, all of the AE signals were of low amplitude, indicating that the spalling failure was caused by the expansion of small-scale cracks. Tensile cracks predominate in the early stages of rockburst, however, when rockburst occurs, a substantial number of shear cracks were formed. Furthermore, the proportion of tensile cracks in the entire spalling failure process was always higher than that of shear cracks.

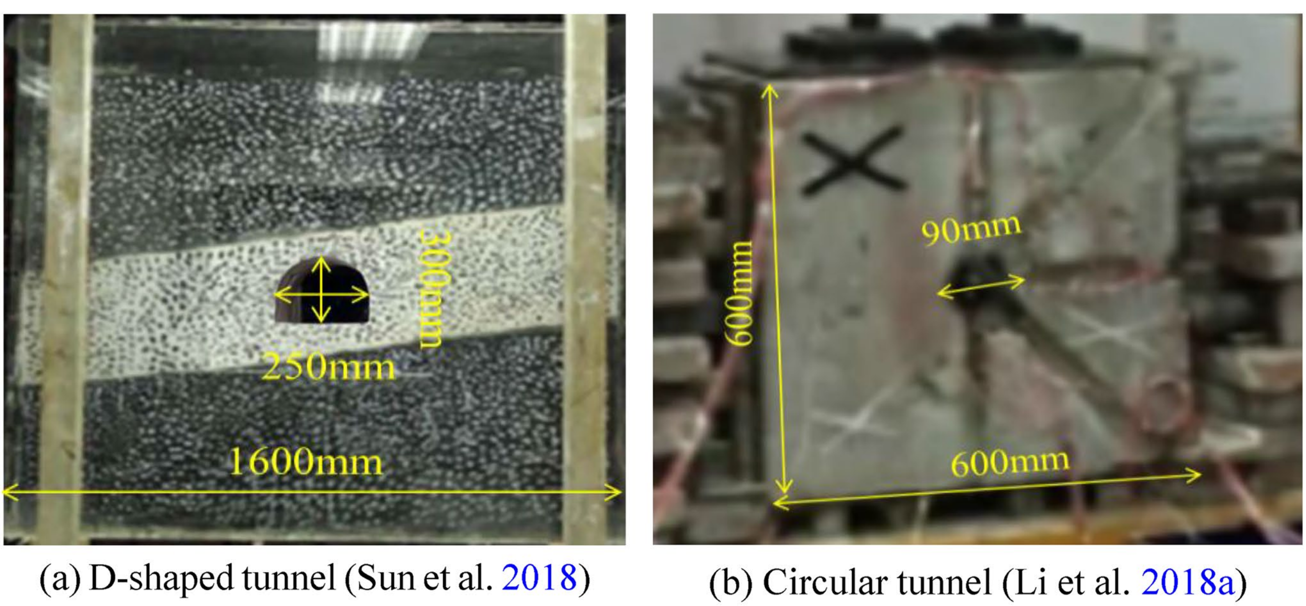

Fig. 26 Large-scale physical model experiment

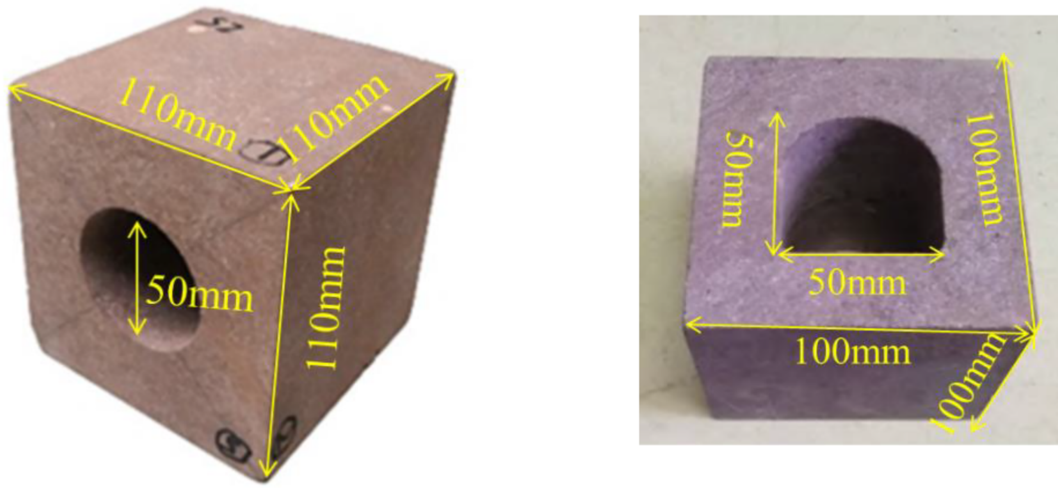

(a) Circular tunnel (Wang et al. 2019) (b) D-shaped tunnel (Gong et al. 2018)

Fig. 27 Small-scale rock block physical model experiment

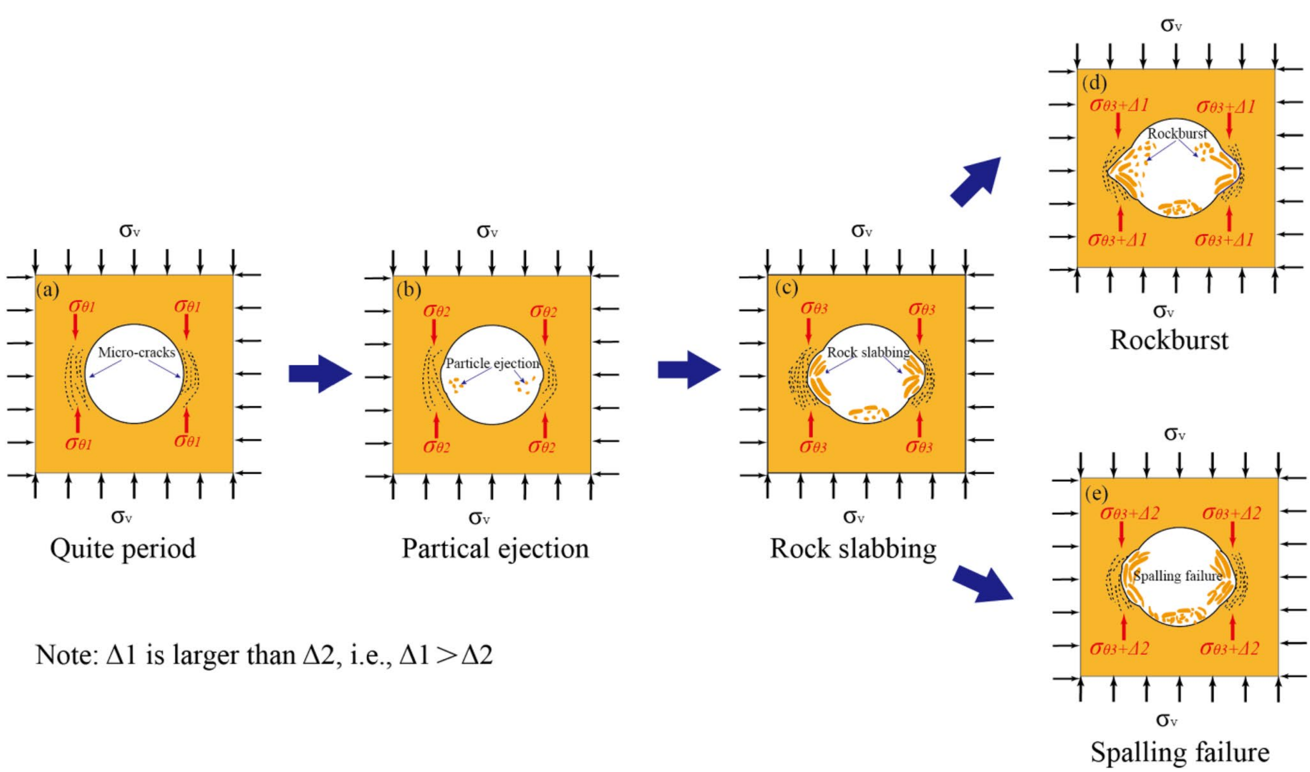

Fig. 28 Schematic diagram of the four stages of rockburst and spalling failure

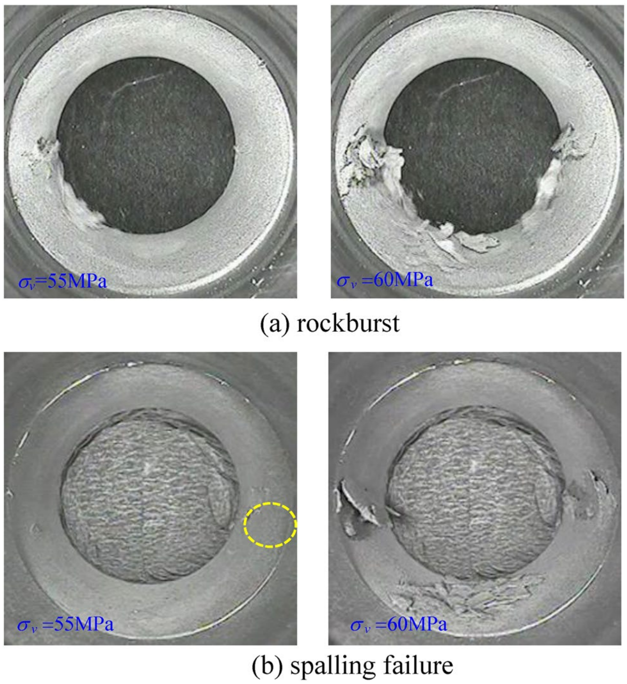

Fig. 29 Failure characteristics of the sidewalls

4. Rockburst produced a greater number of fragments than spalling failure. The fragments of rockburst were in form of long strips, while fragments of spalling failure were in form of flakes or plates. Furthermore, the rockburst pieces had a bigger fractal dimension than the spalling failure fragments, indicating that the rockburst was more severe.

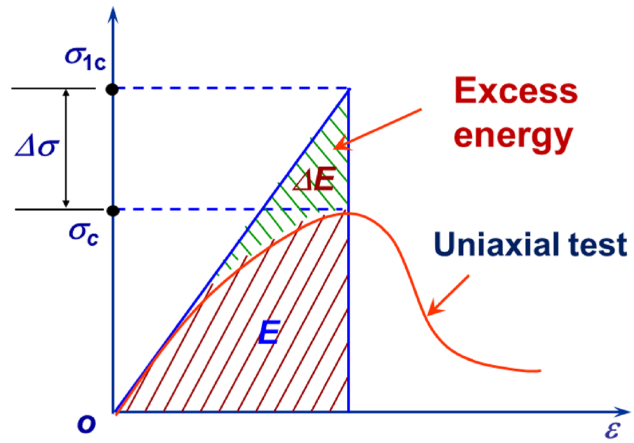

Fig. 30 Energy calculation model (He et al. 2012)

5. Both rockburst and spalling failure generated visible *V*-shaped notches, but their morphological characteristics were different. The angle of rockburst *V*-shaped notches was smaller than that of spalling failure, but the depth was greater. Rockburst had a narrow and deep *V*-shaped notch, whereas spalling failure had a wide and shallow *V*-shaped notch.

Table 6 Strain energy and strain energy density of specimens

	Specimen no.	*X*-strain energy (J)	*Z*-strain energy (J)	*Y*-strain energy (J)	Total strain energy (J)	Strain energy density (kJ/m^3)	
Rockburst	D1	62.27	24.78	318.67	405.72	800.23	798.80
	D2	55.80	15.08	343.48	414.36	817.28	
	D3	61.65	16.36	316.89	394.90	778.90	
Spalling failure	S1	72.09	9.54	294.83	376.46	742.52	739.13
	S2	89.50	11.24	260.85	361.59	711.22	
	S3	83.39	8.33	295.45	387.17	763.64	

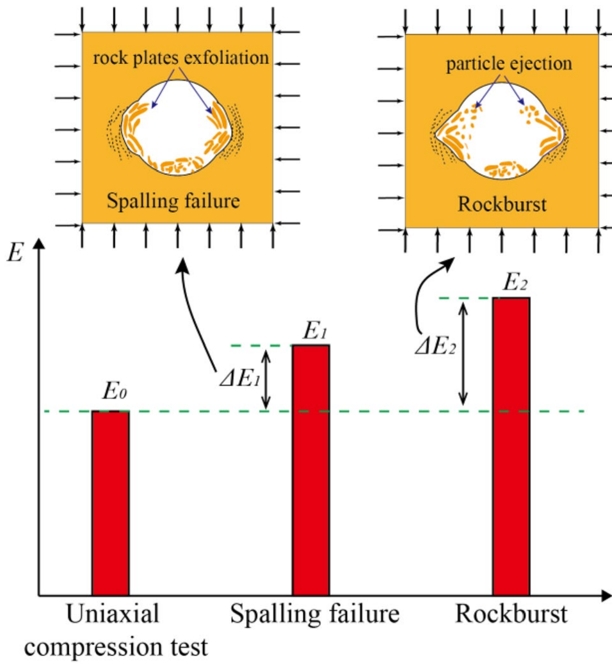

Fig. 31 Schematic illustration of the energy evolution

Author Contributions All authors contributed to the study's conception and design. Material preparation, data collection and analysis were performed by Kai Ling, Yang Wang, Zheng Zhou, Lulu Zhang and Yunpeng Guo. The first draft of the manuscript was written by Kai Ling, Yang Wang, Dongqiao Liu and Manchao He, and all authors commented on previous versions of the manuscript. All authors read and approved the final manuscript.

Funding This research was supported by the National Natural Science Foundation of China (Nos. 52074299 and 41941018), the Fundamental Research Funds for the Central Universities (No. 2021JCCXSB03) and the Fundamental Science Foundation of Institute of Geomechanics (No. DZLXJK202210).

Data availability The datasets used or analysed during the current study are available from the corresponding author on reasonable request.

Declarations

Conflict of interest The authors declare that they have no competing financial interests or personal relationships that could influence the work reported in this paper.

References

Cai M, Kaiser PK, Suorineni F, Su K (2007a) A study on the dynamic behavior of the Meuse/Haute–Marne argillite. Phys Chem Earth 32:907–916

Cai M, Kaiser PK, Morioka H, Minamib M, Maejimab T, Tasakac Y, Kurose H (2007b) FLAC/PFC coupled numerical simulation of AE in large-scale underground excavations. Int J Rock Mech Min Sci 44:550–564

Diederichs MS (2007) The 2003 Canadian Geotechnical Colloquium: mechanistic interpretation and practical application of damage and spalling prediction criteria for deep tunneling. Can Geotech J 44(9):1082–1116

Du K, Tao M, Li XB, Zhou J (2016) Experimental study of slabbing and rockburst induced by true-triaxial unloading and local dynamic disturbance. Rock Mech Rock Eng 49(9):3437–3453

Gong FQ, Si XF (2021) Rockburst simulation tests and strength-weakening effect of circular tunnels under deep high stresses and internal unloading conditions. Chin J Rock Mech Eng 40(2):276–289 (**in Chinese**)

Gong FQ, Luo Y, Si XF, Li XB (2017) Experimental modelling on rockburst in deep hard rock circular tunnels. Chin J Rock Mech Eng 36(7):1634–1648 (**in Chinese**)

Gong FQ, Luo Y, Li XB, Si XF, Tao M (2018) Experimental simulation investigation on rockburst induced by spalling failure in deep circular tunnels. Tunn Undergr Space Technol 81:413–427

Gong FQ, Wu WX, Li TB, Si XF (2019) Experimental simulation and investigation of spalling failure of rectangular tunnel under different three-dimensional stress states. Int J Rock Mech Min Sci 122:104081

Gong FQ, Wu WX, Li TB (2020) Simulation test of spalling failure of surrounding rock in rectangular tunnels with different height-to-width ratios. Bull Eng Geol Env 79:3207–3219

He MC, Miao JL, Feng JL (2010) Rock burst process of limestone and its acoustic emission characteristics under true-triaxial unloading conditions. Int J Rock Mech Min Sci 47(2):286–298

He MC, Xia HM, Jia XN, Gong WL, Zhao F, Liang KY (2012) Studies on classification, criteria and control of rockbursts. J Rock Mech Geotech Eng 4(2):97–114

He MC, e Sousa LR, Miranda T, Zhu GL (2015) Rockburst laboratory tests database—application of data mining techniques. Eng Geol 185:116–130

He MC, Ren FQ, Liu DQ (2018) Rockburst mechanism research and its control. Int J Min Sci Technol 28(5):829–837

He MC, Li JY, Liu DQ, Ling K, Ren FQ (2021a) A novel true triaxial apparatus for simulating strain bursts under high stress. Rock Mech Rock Eng 54(2):759–775

He MC, Ren FQ, Liu DQ, Zhang SD (2021b) Experimental study on strain burst characteristics of sandstone under true triaxial loading and double faces unloading in one direction. Rock Mech Rock Eng 54(1):149–171

He MC, Li JY, Ren FQ, Liu DQ (2021c) Experimental investigation on rockburst ejection velocity of unidirectional double-face unloading of sandstone with different bedding angles. Chin J Rock Mech Eng 40(3):433–447 (**in Chinese**)

Hidalgo KP, Nordlund E (2012) Failure process analysis of spalling failure-comparison of laboratory test and numerical modelling data. Tunn Undergr Space Technol 32:66–77

Hoek E, Martin CD (2014) Fracture initiation and propagation in intact rock—a review. J Rock Mech Geotech Eng 6(4):287–300

Hu XC, Su GS, Chen GY, Mei SM, Feng XT, Mei GX, Huang XH (2019) Experiment on rockburst process of borehole and its acoustic emission characteristics. Rock Mech Rock Eng 52(3):783–802

Hu XC, Su GS, Li ZY, Xu CS, Yan XY, Liu YX, Yan LB (2021) Suppressing rockburst by increasing the tensile strength of rock surface: an experimental study. Tunn Undergr Space Technol 107:103645

Huang LY, Yang SX, Cui XF, Chen QC, Yao R (2013) Analysis of characteristics of measured stress and stability of faults in North China. Rock Soil Mech 34(Supp. 1):204–213 (**in Chinese**)

Keneti A, Sainsbury BA (2018) Review of published rockburst events and their contributing factors. Eng Geol 246:361–373

Lee M, Haimson B (1993) Laboratory study of borehole breakouts in Lac du Bonnet granite: a case of extensile failure mechanism. Int J Rock Mech Min Sci Geomech Abstr 30(7):1039–1045

Li XB, Gong FQ, Tao M, Dong LJ, Du K, Ma CD, Zhou Z, Yin TB (2017) Failure mechanism and coupled static-dynamic loading theory in deep hard rock mining: a review. J Rock Mech Geotech Eng 9(4):767–782

Li TB, Pan HS, Chen GQ, Meng LB (2018a) Physical model tests on thermo-mechanical effects in rockbursts around tunnels. Chin J Rock Mech Eng 37(2):261–273 (**in Chinese**)

Li XB, Feng F, Li DY, Du K, Ranjith PG, Rostami J (2018b) Failure characteristics of granite influenced by sample height-to-width ratios and intermediate principal stress under true-triaxial unloading conditions. Rock Mech Rock Eng 51(5):1321–1345

Li YZ, Su GS, Pang JY, Liu CH, Zhang QH, Yang XF (2021) Mechanism of structural–slip rockbursts in civil tunnels: an experimental investigation. Rock Mech Rock Eng 54(6):2763–2790

Liu CY, Zhao GM, Xu WS, Meng XR, Huang SJ, Zhou J, Wang YK (2020) Experimental investigation on failure process and spatio-temporal evolution of rockburst in granite with a prefabricated circular hole. J Central South Univ 27(10):2930–2944

Liu DQ, Ling K, Li D, He MC, Li JY, Han ZJ, Zhang SD (2021) Evolution of anisotropy during sandstone rockburst process under double-faces unloading. J Central South Univ 28(8):2472–2484

Luo Y, Gong FQ, Li XB, Wang SY (2020) Experimental simulation investigation of influence of depth on spalling characteristics in circular hard rock tunnel. J Central South Univ 27(3):891–910

Ma K, Liu GY (2022) Three-dimensional discontinuous deformation analysis of failure mechanisms and movement characteristics of slope rockfalls. Rock Mech Rock Eng 55(1):275–296

Martin CD (1997) Seventeenth Canadian geotechnical colloquium: the effect of cohesion loss and stress path on brittle rock strength. Can Geotech J 34(5):698–725

Martin CD, Christiansson R (2009) Estimating the potential for spalling around a deep nuclear waste repository in crystalline rock. Int J Rock Mech Min Sci 46(2):219–228

Martin CD, Kaiser PK, Mccreath DR (1999) Hoek–Brown parameters for predicting the depth of brittle failure around tunnels. Can Geotech J 36(1):136–151

Ohno K, Ohtsu M (2010) Crack classification in concrete based on acoustic emission. Constr Build Mater 24(12):2339–2346

Qiu SL, Feng XT, Zhang CQ, Xiang TB (2014) Estimation of rockburst wall-rock velocity invoked by slab flexure sources in deep tunnels. Can Geotech J 51(5):520–539

Si XF, Gong FQ, Luo Y, Li XB (2018) Experimental simulation on rockburst process of deep three-dimensional circular cavern. Rock Soil Mech 39(2):621–634 (**in Chinese**)

Si XF, Huang LQ, Li XB, Ma CD, Gong FQ (2021) Experimental investigation of spalling failure of *D*-shaped tunnel under three-dimensional high-stress conditions in hard rock. Rock Mech Rock Eng 54(6):3017–3038

Si XF, Li XB, Gong FQ, Huang LQ, Liu XL (2022a) Experimental investigation of failure process and characteristics in circular tunnels under different stress states and internal unloading conditions. Int J Rock Mech Min Sci 154:105116

Si XF, Li XB, Gong FQ, Huang LQ, Ma CD (2022b) Experimental investigation on rockburst process and characteristics of a circular opening in layered rock under three-dimensional stress conditions. Tunn Undergr Space Technol 127:104603

Su GS, Jiang JQ, Zhai SB, Zhang GL (2017a) Influence of tunnel axis stress on strainburst: an experimental study. Rock Mech Rock Eng 50(6):1551–1567

Su GS, Zhai SB, Yan LB, Jiang JQ, Zhang GL (2017b) Influence of radial stress gradient on strainbursts: an experimental study. Rock Mech Rock Eng 50(10):2659–2676

Su GS, Hu LH, Feng XT, Yan LB, Zhang GL, Yan SZ, Zhao B, Yan ZF (2018) True triaxial experimental study of rockbursts induced by ramp and cyclic dynamic disturbances. Rock Mech Rock Eng 51(4):1027–1045

Su GS, Jiang JQ, Feng XT, Jiang Q, Chen ZY, Mo JH (2019) Influence of loading rate on strainburst: an experimental study. Bull Eng Geol Env 78(5):3559–3573

Su GS, Gan W, Zhai SB, Zhao GF (2020) Acoustic emission precursors of static and dynamic instability for coarse-grained hard rock. J Central South Univ 27(10):2883–2898

Sun XM, Chen F, Miao CY, Song P, Li G, Zhao CW, Xia X (2018) Physical modeling of deformation failure mechanism of surrounding rocks for the deep-buried tunnel in soft rock strata during the excavation. Tunn Undergr Space Technol 74:247–261

Wang Y, He MC, Liu DQ, Gao YB (2019a) Rockburst in sandstone containing elliptic holes with varying axial ratios. Adv Mater Sci Eng 2019:5169618

Wang Y, Zhu C, He MC, Liu DQ, Lin YW, Du SL (2019b) Fragmentation characteristics analysis of sandstone fragments for impact rockburst under different dynamic loading frequency. Geotech Geol Eng 37:2715–2727

Zhang YB, Wu WR, Yao XL, Liang P, Sun L, Liu XX (2019) Study on spectrum characteristics and clustering of acoustic emission signals from rock fracture. Circ Syst Signal Process 39(2):1133–1145

Zhao J (2000) Applicability of Mohr–Coulomb and Hoek–Brown strength criteria to the dynamic strength of brittle rock. Int J Rock Mech Min Sci 37(7):1115–1121

Zhao HG, Liu C, Huang G, Yu BC, Liu YB, Song ZL (2020) Experimental investigation on rockburst process and failure characteristics in trapezoidal tunnel under different lateral stresses. Constr Build Mater 259:119530

Publisher's Note Springer Nature remains neutral with regard to jurisdictional claims in published maps and institutional affiliations.